YALE
PEABODY
MUSEUM

JOURNAL OF MARINE RESEARCH

The *Journal of Marine Research,* one of the oldest journals in American marine science, published important peer-reviewed original research on a broad array of topics in physical, biological, and chemical oceanography vital to the academic oceanographic community in the long and rich tradition of the Sears Foundation for Marine Research at Yale University.

An archive of all issues from 1937 to 2021 (Volume 1–79) are available through EliScholar, a digital platform for scholarly publishing provided by Yale University Library at https://elischolar.library.yale.edu/.

Requests for permission to clear rights for use of this content should be directed to the authors, their estates, or other representatives. The *Journal of Marine Research* has no contact information beyond the affiliations listed in the published articles. We ask that you provide attribution to the *Journal of Marine Research.*

Yale University provides access to these materials for educational and research purposes only. Copyright or other proprietary rights to content contained in this document may be held by individuals or entities other than, or in addition to, Yale University. You are solely responsible for determining the ownership of the copyright, and for obtaining permission for your intended use. Yale University makes no warranty that your distribution, reproduction, or other use of these materials will not infringe the rights of third parties.

Linear ocean circulation theory with realistic bathymetry

by Rick Salmon[1]

ABSTRACT

The linear equations governing stratified, wind-driven flow in an ocean of arbitrary shape may be combined into a single ''advection-diffusion' equation for the pressure ϕ, in which the ''flow'' advecting ϕ includes a delta-function contribution at the ocean bottom in the sense of southward ''advection'' of ϕ along western continental slopes. This interpretation of the ϕ-equation helps to explain numerical solutions obtained with a finite-element model incorporating realistic North Atlantic bathymetry.

1. Introduction

In this paper, we examine numerical solutions of the three-dimensional, linear equations (2.1) governing stratified, wind-driven ocean circulation that departs only slightly from a state of rest with Vaisala frequency N. The momentum equations (2.1a–c) omit the advection of momentum, and the buoyancy equation (2.1d) retains only the vertical advection of the mean buoyancy gradient N^2. Wind forcing enters as a body force acting near the ocean surface. Rayleigh friction and Newtonian cooling provide the only dissipation. The only boundary condition is no-normal-flow. We solve (2.1) approximately, by the method of finite elements, in a domain resembling the North Atlantic. The finite elements conform to the ocean bottom and the coastline, and the vertical resolution is greatest near the ocean surface and bottom, and in the shallow water near the coast. For a quick impression of the model, see Figures 7, 13 and 19.

This paper, which is confined to linear theory, represents the first step in the development of high-resolution, finite-element ocean circulation models based on the planetary geostrophic equations (the inertia-less equations with full, nonlinear buoyancy advection) and on the form of the (inertia-containing) semigeostrophic equations proposed by Salmon (1996). The linear solutions described herein demonstrate the accuracy of the finite-element approximation and form a baseline for future comparison with the more sophisticated dynamical models under development. However, the linear solutions are also interesting in their own right: Although oceanographers have long recognized the shortcomings of linear ocean circulation theory, it is by no means trivial, and it is still the source of most of what we actually *understand* about ocean circulation. However, linear theory is usually applied to ocean basins with very ideal shapes—the case of a rectangular ocean basin with a flat bottom being typical—and extensions of the theory normally proceed in

1. Scripps Institution of Oceanography, La Jolla, California, 92093-0225, U.S.A.

the direction of increasing sophisticated dynamics, with no increase in the complexity of the geometry. In this paper, we extend flat-bottom linear theory in the opposite direction, to ocean basin shapes of realistic complexity, with no increase in the complexity of the dynamics, and hence no loss in our ability to understand the physics. Our purpose is not to inflate or defend linear theory, but to understand its results and limitations as completely as possible.

Welander (1968) recognized a useful analogy between the equation governing the transport streamfunction ψ in linear ocean circulation theory and the advection-diffusion equation for a passive scalar. In Welander's analogy, the streamfunction ψ is "advected" by a "velocity field" with "streamfunction" f/H, where f is the Coriolis parameter and H is the depth of the ocean. Although Welander considered topography of large horizontal scale, his analogy applies to arbitrary $H(x, y)$ and is in fact most useful on western continental slopes, where ψ is large and the "streamfunction" f/H varies rapidly.

In Section 2, we show that Welander's analogy applies to the fully three-dimensional equations for linear ocean circulation. The pressure $\phi(x, y, z)$ replaces $\psi(x, y)$ as the "advected" scalar, and the "advecting velocity" includes a delta-function contribution at the ocean bottom, corresponding to a southward "flow" along isobaths on western continental slopes.

In Section 3, we use boundary-layer theory and the extended Welander analogy to understand the bottom boundary layers that appear in finite-element solutions of the linear dynamics in a three-dimensional domain containing an idealized western continental slope. Then, letting $N \to 0$, we show how these solutions approach the more familiar solution for a homogeneous fluid.

In Sections 4 and 5, we examine linear, finite-element solutions that incorporate realistic North Atlantic bathymetry. The structure of the model, and, particularly, the way in which the finite-element grid concentrates vertical resolution near the ocean bottom and in shallow water, allow us to probe the physically revealing regime of asymptotically small friction. Concentrating on the complex region around the Caribbean Sea and the Gulf of Mexico, we compare a solution driven by wind stress over the whole North Atlantic to other solutions in which the wind curl is switched off near the western boundary. We find that the total linear circulation can be understood as a response to local wind forcing, and to the "advection" of pressure, westward through Caribbean passages, and pseudosouthward along isobaths in the bottom boundary layers.

2. Linear dynamics and the advection-diffusion analogue

The linearized equations of motion, in dimensional form and in Cartesian coordinates, are

$$-fv = -\frac{\partial \phi}{\partial x} - \varepsilon u + \frac{\partial \tau^x}{\partial z} \tag{2.1a}$$

$$+ fu = -\frac{\partial \phi}{\partial y} - \varepsilon v + \frac{\partial \tau^y}{\partial z} \tag{2.1b}$$

$$0 = -\frac{\partial \phi}{\partial z} + \theta \tag{2.1c}$$

$$wN^2 = -k\theta \tag{2.1d}$$

$$\frac{\partial u}{\partial x} + \frac{\partial v}{\partial y} + \frac{\partial w}{\partial z} = 0. \tag{2.1e}$$

Here, (u, v, w) is the velocity in the (east, north, up) direction with coordinate (x, y, z), $f = \beta y$ is the Coriolis parameter, and ϕ is the pressure (divided by a constant representative density ρ_0). θ is the buoyancy *anomaly,* the departure of the full buoyancy

$$\overline{\theta}(z) + \theta(x, y, z) \equiv -g \frac{(\rho_\theta - \rho_0)}{\rho_0} = -g 10^{-3} \sigma_\theta \tag{2.2}$$

from the mean value $\overline{\theta}(z)$ with vertical derivative $d\overline{\theta}/dz \equiv N^2(z)$. g is the gravity constant. ρ_θ is the potential density. The constants ε and k are damping coefficients for horizontal momentum and buoyancy, respectively. Despite the extreme simplicity of the damping terms, solutions of (2.1) remain smooth because (2.1) omit the (nonlinear) advection of momentum and buoyancy. However, Rayleigh friction (that is, the ε-terms in (2.1a–b)) accommodates only the boundary condition of no-normal-flow at rigid boundaries.

The impossibility of a stress boundary condition at the ocean surface means that the wind forcing must be imposed as a body force acting within a thin layer near the surface. Thus the $\tau(x, y, z)$-terms in (2.1) are prescribed body-forcing terms. In this paper, we consider only wind forcing. However, heating terms could be added to (2.1d), and, because (2.1) are linear equations, the wind-driven and thermally driven solutions could be superposed.

The greatest shortcoming of linear ocean circulation theory is its neglect of the horizontal buoyancy advection in (2.1d). (This shortcoming is common to all models that linearize about a state of rest, and has nothing to do with the especially simple dissipation terms advocated here.) Because of this neglect, the vertical velocity and, more importantly, the vertical vortex stretching can be significant only in regions in which the diabatic term—the right-hand side of (2.1d)—is significant.

The general properties of (2.1), including the motivation for, and the special advantages of, the Rayleigh friction have been discussed in previous papers; see, for example, Salmon (1994). A primary advantage of (2.1) is that the five equations can be combined into a single equation for ϕ with an illuminating interpretation. First, we use (2.1a–d) to express

the velocity in terms of the pressure derivatives,

$$u = -\frac{f}{f^2 + \varepsilon^2}\frac{\partial\phi}{\partial y} - \frac{\varepsilon}{f^2 + \varepsilon^2}\frac{\partial\phi}{\partial x} + u^\tau$$

$$v = +\frac{f}{f^2 + \varepsilon^2}\frac{\partial\phi}{\partial x} - \frac{\varepsilon}{f^2 + \varepsilon^2}\frac{\partial\phi}{\partial y} + v^\tau \qquad (2.3)$$

$$w = -\frac{k}{N^2}\frac{\partial\phi}{\partial z}.$$

Here

$$\mathbf{u}^\tau(x, y, z) \equiv (u^\tau, v^\tau) \equiv \frac{1}{(f^2 + \varepsilon^2)}\left(f\frac{\partial\tau^y}{\partial z} + \varepsilon\frac{\partial\tau^x}{\partial z}, -f\frac{\partial\tau^x}{\partial z} + \varepsilon\frac{\partial\tau^y}{\partial z}\right) \qquad (2.4)$$

is the prescribed *forcing velocity*. Away from the equator, that is, where $f^2 \gg \varepsilon^2$, we may regard $\mathbf{u}^\tau$ as the Ekman correction velocity. Substituting (2.3) into the continuity equation (2.1e), we obtain a single elliptic equation,

$$J\left(\phi, \frac{f}{f^2 + \varepsilon^2}\right) = \nabla \cdot \left(\frac{\varepsilon}{f^2 + \varepsilon^2}\nabla\phi\right) + \frac{\partial}{\partial z}\left(\frac{k}{N^2}\frac{\partial\phi}{\partial z}\right) + W, \qquad (2.5)$$

for the pressure $\phi(x, y, z)$. Here $J(A, B) \equiv A_x B_y - A_y B_x$ is the horizontal Jacobian, $\nabla \equiv (\partial_x, \partial_y)$ is the horizontal gradient operator, and

$$W = -\nabla \cdot \mathbf{u}^\tau. \qquad (2.6)$$

The no-normal-flow boundary conditions,

$$w = 0 \qquad \text{at} \qquad z = 0 \qquad (2.7)$$

and

$$w = -u\frac{\partial H}{\partial x} - v\frac{\partial H}{\partial y} \qquad \text{at} \qquad z = -H(x, y) \qquad (2.8)$$

take the forms

$$\frac{\partial\phi}{\partial z} = 0 \quad \text{at} \qquad z = 0 \qquad (2.9)$$

and

$$-\frac{k}{N^2}\frac{\partial\phi}{\partial z} = \frac{f}{f^2 + \varepsilon^2}J(H, \phi) + \frac{\varepsilon}{f^2 + \varepsilon^2}\nabla\phi \cdot \nabla H - \mathbf{u}^\tau \cdot \nabla H \quad \text{at} \qquad z = -H(x, y). \qquad (2.10)$$

We shall assume that the ocean depth $H(x, y)$ vanishes smoothly at the coastlines, but it is easy to write the corresponding boundary condition at vertical sidewalls (which corresponds to the limit of infinite ∇H in (2.10)).

Now, (2.5) fits the form

$$\mathbf{U} \cdot \nabla \phi = -\nabla \cdot \mathbf{F} + W \tag{2.11}$$

of an advection-diffusion equation for the pressure ϕ. The "advecting velocity" is

$$\mathbf{U} \equiv -\frac{\hat{\beta}}{\hat{f}^2} \mathbf{i}, \tag{2.12}$$

where

$$\hat{f} \equiv \frac{f^2 + \varepsilon^2}{f},$$

$$\hat{\beta} \equiv \frac{d\hat{f}}{dy}, \tag{2.13}$$

and $\mathbf{i}$ is the unit vector in the eastward direction. The "diffusive flux" is

$$\mathbf{F} \equiv -\kappa_h \nabla \phi - \kappa_v \frac{\partial \phi}{\partial z} \mathbf{k}, \tag{2.14}$$

where

$$\kappa_h \equiv \frac{\varepsilon}{(f^2 + \varepsilon^2)} \quad \text{and} \quad \kappa_v \equiv \frac{k}{N^2} \tag{2.15}$$

are the horizontal and vertical "diffusion coefficients," respectively. W is the "source." (Throughout this paper, we use quotation marks when referring to the advection-diffusion analog. Thus "advection" refers to the transport of ϕ by the "velocity field" $\mathbf{U}$.) The surface boundary condition (2.9) corresponds to "no flux" of ϕ through the ocean surface. However, the bottom boundary condition (2.10) is harder to interpret because of the first (Jacobian) term on its right-hand side. Without this Jacobian term, (2.10) would correspond to a boundary condition of prescribed normal "diffusive flux" $\mathbf{F} \cdot \mathbf{n}$, where $\mathbf{n}$ is the unit normal to the ocean bottom. Clearly the Jacobian term in (2.10) complicates the interpretation of (2.5, 9–10) as an advection-diffusion problem.

By a mathematical trick, we can lift the conceptually troublesome Jacobian term out of the bottom boundary condition (2.10) and place it into the interior equation (2.5). This greatly facilitates the interpretation of the solutions of (2.5, 2.9–10). We proceed somewhat indirectly, first introducing an expression that will be useful in the numerical formulation of

the problem. First note that the continuity equation (2.1e), namely,

$$\nabla_3 \cdot \mathbf{v} = 0 \tag{2.16}$$

and no-normal-flow boundary conditions are together equivalent to the statement that

$$\frac{\delta I}{\delta \alpha} = 0, \tag{2.17}$$

where

$$I \equiv \iiint dx\, dy\, dz\, \{\mathbf{v} \cdot \nabla_3 \alpha\}. \tag{2.18}$$

Here $\mathbf{v} \equiv (\mathbf{u}, w) \equiv (u, v, w)$ is the three-dimensional fluid velocity, $\nabla_3 \equiv (\nabla, \partial_z) \equiv (\partial_x, \partial_y, \partial_z)$ is the three-dimensional gradient operator, $\alpha(x, y, z)$ is a *test function,* and $\delta/\delta\alpha$ denotes the functional derivative with respect to α. The integration in (2.18) is over the whole volume of the ocean. In other words, the requirement that

$$\delta I = \iiint dx\, dy\, dz\, (\mathbf{v} \cdot \nabla_3 \delta\alpha) = -\iiint dx\, dy\, dz\, \delta\alpha(\nabla_3 \cdot \mathbf{v}) + \oiint dA\, \delta\alpha\, \mathbf{v} \cdot \mathbf{n} \tag{2.19}$$

vanish for arbitrary $\delta\alpha(x, y, z)$ implies that $\nabla_3 \cdot \mathbf{v} = 0$ throughout the body of the fluid and that $\mathbf{v} \cdot \mathbf{n} = 0$ at its boundaries, where $\mathbf{n}$ is the outward-pointing unit normal. (Since I is linear in α, we can also say that the physics is equivalent to the requirement that (2.18) vanish for arbitrary $\alpha(x, y, z)$.) Using (2.3), we write the integral (2.18) as a functional of ϕ and α in the form

$$I[\phi, \alpha] = \iiint dx\, dy\, dz\, \left\{ \frac{f}{f^2 + \varepsilon^2} J(\phi, \alpha) - \frac{\varepsilon}{f^2 + \varepsilon^2} \nabla\phi \cdot \nabla\alpha - \frac{k}{N^2} \frac{\partial\phi}{\partial z} \frac{\partial\alpha}{\partial z} + \mathbf{u}^\tau \cdot \nabla\alpha \right\}, \tag{2.20}$$

Then the requirement $\delta I/\delta\alpha = 0$ yields the pressure-equation (2.5) and the boundary conditions (2.9–10).

Now consider the first term on the right-hand side of (2.20). It is this term that leads to the Jacobian terms in (2.5) and (2.10). Integrating by parts and making use of the divergence theorem, we rewrite the Jacobian term in (2.20) in the form

$$\iiint dx\, dy\, dz\, \left\{ \frac{1}{\hat{f}} J(\phi, \alpha) \right\} = \iiint dx\, dy\, dz\, \left\{ -\alpha J\left(\phi, \frac{1}{\hat{f}}\right) + J\left(\phi, \frac{\alpha}{\hat{f}}\right) \right\}$$

$$= \iiint dx\, dy\, dz\, \left\{ \alpha J\left(\frac{1}{\hat{f}}, \phi\right) \right\} + \iint dx\, dy\, \left\{ \frac{\alpha_b}{\hat{f}} J(H, \phi_b) \right\} \tag{2.21}$$

where $\hat{f}$ is defined by (2.13a), and $\alpha_b = \alpha(x, y, -H(x, y))$ and $\phi_b = \phi(x, y, -H(x, y))$ are the test function and the pressure evaluated at the ocean bottom, respectively. The last term in (2.21) contributes the conceptually troublesome Jacobian term to the bottom boundary condition (2.10). To remove this term from the boundary condition, we rewrite the last term

in (2.21) as

$$\iiint dx\, dy\, dz \left\{\frac{\alpha}{\hat{f}} J(H, \phi)\, \delta(z + H(x, y))\right\} \tag{2.22}$$

where $\delta(\ )$ denotes the delta-function. Then (2.20) becomes

$$I = \iiint dx\, dy\, dz \left\{\alpha J\left(\frac{1}{\hat{f}}, \phi\right) + \frac{\alpha}{\hat{f}} J(H, \phi)\, \delta(z + H)\right.$$

$$\left. - \frac{\varepsilon}{f^2 + \varepsilon^2} \nabla\phi \cdot \nabla\alpha - \frac{k}{N^2} \frac{\partial\phi}{\partial z} \frac{\partial\alpha}{\partial z} + \mathbf{u}^\tau \cdot \nabla\alpha\right\}. \tag{2.23}$$

The requirement that $\delta I/\delta\alpha = 0$ now yields an advection-diffusion equation of the form (2.11) but with the "advecting velocity" given by

$$\mathbf{U} \equiv -\frac{\hat{\beta}}{\hat{f}^2}\mathbf{i} + \frac{1}{\hat{f}}\left(\frac{\partial H}{\partial y}, -\frac{\partial H}{\partial x}\right)\delta(z + H) \tag{2.24}$$

instead of (2.12). The top boundary condition (2.9) is unchanged, but the bottom boundary condition (2.10) is replaced by

$$-\frac{k}{N^2}\frac{\partial\phi}{\partial z} = \frac{\varepsilon}{f^2 + \varepsilon^2}\nabla\phi \cdot \nabla H - \mathbf{u}^\tau \cdot \nabla H \qquad \text{at} \qquad z = -H(x, y), \tag{2.25}$$

which contains no Jacobian term.

Of course, the formulation (2.5, 9–10) is mathematically equivalent to (2.9, 11, 24–25). However, the latter formulation, in which the "advecting velocity" (2.24) contains the delta-function contribution at the ocean bottom, is much easier to interpret by analogy with the advection-diffusion of a scalar. When the delta-contribution appears in the "advecting velocity," the boundary conditions (2.9) and (2.25) both take the form

$$\mathbf{F} \cdot \mathbf{n} = -\mathbf{u}^\tau \cdot \mathbf{n}, \tag{2.26}$$

where $\mathbf{F}$ is given by (2.14). The right-hand side of (2.26) corresponds to a prescribed "diffusive flux." This "flux" vanishes at the ocean surface (where $\mathbf{n} = \mathbf{k}$) and on those portions of the bottom that lie below the thin surface layer of nonzero prescribed wind forcing.

The delta-term in (2.24) corresponds to a sheet of "current" "advecting" ϕ along the ocean bottom in a direction parallel to the isobaths, with deep water to the left in the northern hemisphere, that is, in a southward direction on western continental slopes. The speed of this "bottom advection sheet" is proportional to the bottom slope. In contrast, the beta-contribution to (2.24) corresponds to a westward "advection" of ϕ within the

body of the fluid, except at very low latitudes ($f^2 < \varepsilon^2$) where

$$\hat{\beta} = \beta\left(1 - \frac{\varepsilon^2}{f^2}\right)$$

(2.27)

becomes negative and the beta-contribution corresponds to a strong *eastward* "advection" of ϕ along the equator.

Away from the equator, the westward "beta advection" in the body of the fluid corresponds to the westward propagation of Rossby waves. The eastward "advection" along the equator (with maximum "speed" β/ε^2 on the equator) corresponds to the eastward propagation of equatorial Kelvin waves. The "advection" of ϕ by the "bottom advection sheet" corresponds to the propagation of bottom-trapped Rossby waves. These three "advections" correspond to the uni-directional waves present in solutions of the time-dependent, undamped form of (2.1). By interpreting (2.11, 24) as an advection-diffusion problem for ϕ in which these three "advections" participate, we can understand the solutions of (2.1) rather easily. Once the pressure $\phi(x, y, z)$ is known, the fluid velocities (2.3) and the buoyancy anomaly $\theta = \partial\phi/\partial z$ are determined.

If, instead of the ε- and κ-terms, (2.1) had contained the more conventional (Laplacian) diffusion of buoyancy and momentum, then the analogue of (2.5) would contain biharmonic diffusion terms. These biharmonic diffusion terms and accompanying additional boundary conditions would make numerical solution much more difficult, but the results would be qualitatively similar to the solutions presented in this paper. If the dynamics include nonlinear advection of momentum and buoyancy, then the momentum and buoyancy equations *must* contain Laplacian diffusion terms, or the solutions would cease to be smooth. However, in the absence of nonlinear advection terms, it seemed appealing to let the dissipative terms in (2.1) take the simplest conceivable form.

Because of the decay term in (2.1d), which restores the buoyancy to the prescribed mean state represented by N, we must interpret the model buoyancy field carefully. The boundary condition that $w = 0$ at the sea surface implies that $\theta = 0$ there. Thus the surface buoyancy is horizontally uniform, and it is the buoyancy at the bottom of the Ekman layer (where w is relatively large) that should probably be compared to the observed surface temperature, or to the surface temperature in a linear model with vertical diffusion.

Although the pressure equation with advection-diffusion analogy offers the best means of understanding the solutions of (2.1), it is somewhat more conventional to formulate the problem in terms of the streamfunction ψ for the depth-integrated flow, defined by

$$\int_{-H}^0 \mathbf{u}\, dz = \left(-\frac{\partial\psi}{\partial y}, \frac{\partial\psi}{\partial x}\right).$$

(2.28)

By cross-differentiating the vertically integrated horizontal momentum equations to remove the vertically integrated pressure, we obtain the familiar equation,

$$J(f, \psi) = J(H, \phi_b) + \varepsilon\nabla^2\psi - curl\,(\Delta\tau),$$

(2.29)

where ϕ_b is the pressure at the bottom, *curl* denotes the vertical component of the curl $(\mathbf{k} \cdot \nabla \times)$, and $\Delta \tau = \tau_s - \tau_b$ is the difference between the prescribed stress at the surface and bottom of the ocean. Alternatively,

$$J\left(\frac{f}{H}, \psi\right) = J\left(\frac{1}{H}, \gamma\right) + \varepsilon \nabla \cdot \left(\frac{1}{H}\nabla\psi\right) - curl\ (\Delta\tau/H), \qquad (2.30)$$

where

$$\gamma = -\int_{-H}^{0} z\theta\ dz. \qquad (2.31)$$

The first term on the right-hand side of (2.29) represents the torque exerted by the sloping bottom. The first term on the right-hand side of (2.30)—the so-called *jebar* term— represents the contribution of the *non*-depth-averaged pressure to this bottom torque; the full bottom torque is spread among all the terms in (2.30).

In the case of a flat bottom (uniform H) or homogeneous fluid (uniform θ), the *jebar* term vanishes, and (2.30) reduces to a closed advection-diffusion equation,

$$J\left(\frac{f}{H}, \psi\right) = \nabla \cdot \left(\frac{\varepsilon}{H}\nabla\psi\right) - curl\ (\Delta\tau/H) \qquad (2.32)$$

for the streamfunction ψ. The "advecting velocity" has "streamfunction" f/H. This is the equation considered by Welander (1968).

Now consider a homogeneous, rectangular ocean with continental shelves and slopes at the western, northern, and eastern boundaries, and southern boundary along the equator, as shown in Figure 1a. The governing equation is (2.32). The "flow" advecting ψ is pseudowestward along lines of constant f/H that emanate from the southeast corner of the basin and converge on the southwest corner (Fig. 1b). The streamfunction corresponding to a two-gyre wind stress (Fig. 1d) clearly shows the effects of the "advection" toward the southwestern corner of the basin. In the case of a flat bottom (Fig. 1c) this "advection" is everywhere exactly westward, and an ε/β-thickness boundary layer enforces the boundary condition $\psi = 0$ at the western boundary. However, since the "advection" along f/H-lines is everywhere parallel to the coastlines in Figure 1d, the ε-term in (2.32) is important only near the southwestern point of converging f/H-lines. Apart from this corner region, no frictional boundary layers are present in Figure 1d. The western boundary current widths in Figure 1d are determined solely by the convergence of isobaths, and are independent of ε as $\varepsilon \to 0$. For further discussion of homogeneous wind-driven flow over bottom topography, see Becker and Salmon (1997) and references therein.

In the general case of nonuniform θ, *jebar* does not vanish, and (2.30) is no longer a closed equation for ψ. In that case, it seems better to reformulate the entire problem as a three-dimensional equation for ϕ. If the delta-function trick is used to express this three-dimensional problem in the form (2.11, 24, 26), then the interpretation of (2.11) as an advection-diffusion equation is closely analogous to Welander's interpretation of (2.32).

The case of homogeneous fluid corresponds to the limit $k \to \infty$ (or $N \to 0$) in (2.1) and (2.5, 10).

In Section 3, we consider fully three-dimensional solutions of the ϕ-equation in an idealized coastal geometry very similar to that of Figure 1a. We show how boundary-layer theory refines our essentially qualitative interpretation of the ϕ-equation as an advection-diffusion equation, and we investigate the way in which the three-dimensional solutions approach the limit represented by Figure 1d as $k \to \infty$. Then, in Sections 4 and 5, we consider solutions of the ϕ-equation with realistic wind forcing and North Atlantic bathymetry. Even in this much more complex geometry, we find that the viewpoint developed in Sections 2 and 3 offers a fairly complete qualitative explanation of the results.

3. Some idealized solutions

In the linear theory based on (2.5), the "source"-term W drives the ocean circulation. This "source" vanishes below the *Ekman layer*—the thin surface layer of nonzero prescribed $\tau(x, y, z)$. Below the Ekman layer and away from the equator, the balance in (2.5) is between "westward advection" and "downward diffusion,"

$$-\frac{\beta}{f^2}\frac{\partial \phi}{\partial x} = \frac{\partial}{\partial z}\left(\frac{k}{N^2}\frac{\partial \phi}{\partial z}\right).$$
(3.1)

leading to a surface layer of relatively large ϕ—the main thermocline—that thickens toward the west. By the analogy between (3.1) and an advection-diffusion equation (or, by the interpretation of (3.1) as a heat equation in which negative x is the time-like coordinate), the thermocline thickness at distance x from the western boundary is

$$\delta = \sqrt{\frac{kf^2(L - x)}{\beta N^2}}$$
(3.2)

where L is the width of the ocean, and hence $L - x$ is the distance from the eastern boundary.

At most places east of the western continental slope, the ocean bottom lies below the thermocline depth. Since ϕ is small below the thermocline, the bottom-torque is small in water deeper than δ. Therefore, the ocean circulation east of the western continental slope is nearly the same as if the ocean bottom were flat. However, the δ-thickness thermocline layer of large ϕ must intersect the ocean bottom along the western continental slope. There the "bottom advection sheet" "advects" ϕ southward along isobaths near the bottom, and the resulting ocean circulation differs significantly from the flat-bottom case.

In this section, we consider the flow within a narrow western boundary region containing an idealized shelf and slope like that in Figure 1a. We imagine the flow within this western region to be driven by a prescribed pressure, $\phi_E(y, z)$, at its eastern edge. The prescribed pressure $\phi_E(y, z)$ represents the effect of wind forcing on the interior ocean. Within the
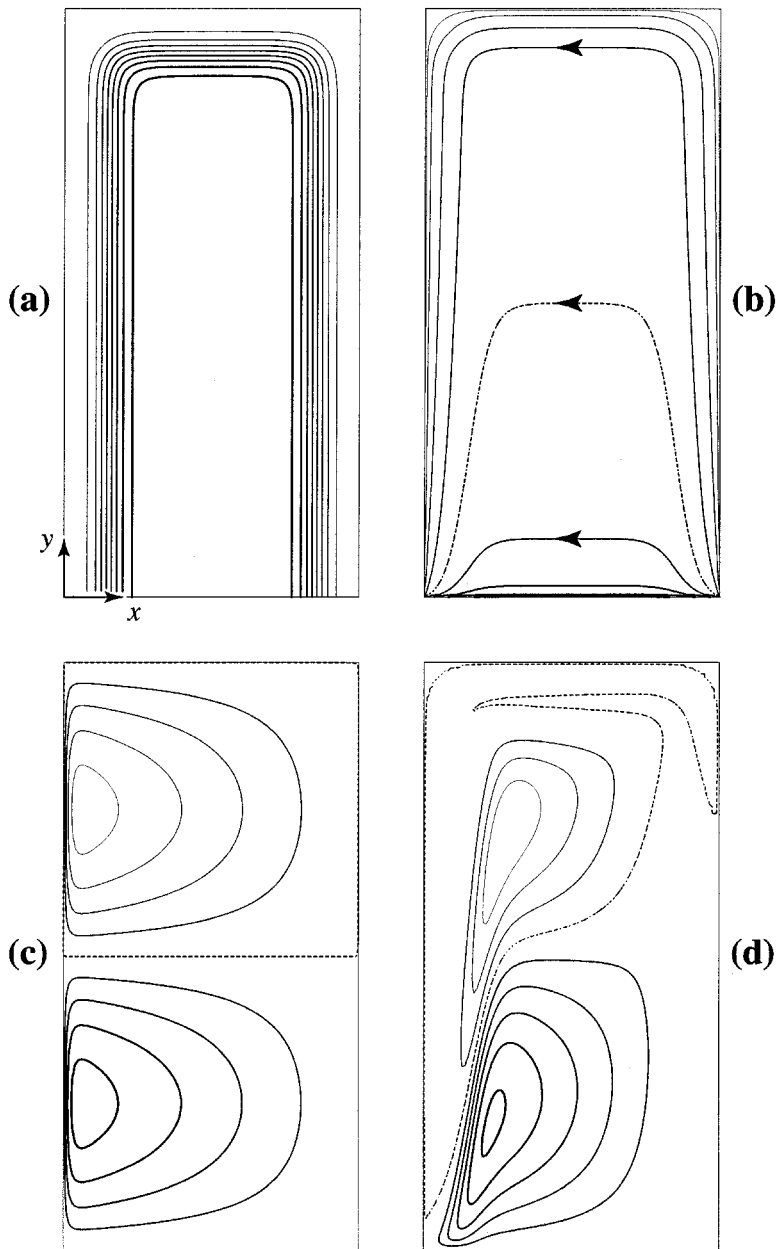
Figure 1. (a) The isobaths in a rectangular ocean with continental slopes along the western, northern and eastern boundaries. The southern boundary is the equator. (b) The corresponding lines of constant f/H, with arrows denoting the direction in which the streamfunction ψ is "advected" according to (2.32). (c) The streamfunction satisfying (2.32) in a homogeneous ocean with a flat bottom and a two-gyre wind curl. (d) The corresponding streamfunction for the bathymetry in (a). The friction coefficient ε has the same small value in both cases (c) and (d). In (c) friction is important in the western boundary layer, but in (d) friction is important only near the southwestern point at which the "flow" in (b) converges.

western boundary region containing the continental slope, we take the local wind forcing to be negligible.

Omitting the wind forcing, and taking N^2 to be a constant (for convenience), we rewrite (2.1) in the *nondimensional* form

$$-fv = -\frac{\partial \phi}{\partial x} - \varepsilon u$$

$$+ fu = -\frac{\partial \phi}{\partial y} - \varepsilon v$$

$$0 = -\frac{\partial \phi}{\partial z} + \theta \tag{3.3}$$

$$w = -\kappa \theta$$

$$\frac{\partial u}{\partial x} + \frac{\partial v}{\partial y} + \frac{\partial w}{\partial z} = 0$$

in which $f = y$, and κ replaces k/N^2. We take ε and κ to be small dimensionless constants and seek solutions of (3.3) in the western boundary region

$$0 < x < \tfrac{1}{4}, \qquad 0 < y < 1, \qquad -H(x) < z < 0 \tag{3.4}$$

in which the fluid depth

$$H(x) = \frac{\tanh (-2 + 16x) - \tanh (-2)}{\tanh (2) - \tanh (-2)} \tag{3.5}$$

depends only on eastward distance and corresponds to the smooth bottom profile shown in Figure 3. The northern ($y = 1$) and southern ($y = 0$, equatorial) boundaries are rigid vertical walls with boundary conditions of no-normal-flow. At the eastern ($x = \tfrac{1}{4}$) edge of (3.4), we require that $\phi = \phi_E(y, z)$, where

$$\phi_E(y, z) = \begin{cases} 0, & 0 < y < \tfrac{1}{3} \\ -\sin (3\pi(y - \tfrac{2}{3})) \exp (-(z/0.5)^2), & \tfrac{1}{3} < y < 1 \end{cases} \tag{3.6}$$

is shown in Figure 4d.

Once again, we regard the domain (3.4) as the thin western boundary region in an ocean extending far to the east. Wind forcing on the ocean interior creates the pressure field (3.6) at the open boundary, $x = \tfrac{1}{4}$. The pressure field (3.6) corresponds to a cyclonic wind gyre in the northern third of the ocean basin, an anticyclonic gyre in the middle third, and quiescent wind in the southern third of the ocean. At the open boundary, the thermocline occupies the upper half of the water column. We anticipate that the β-term in (3.1) "advects" the open-boundary pressure (3.6) westward toward the continental slope. There ϕ experiences strong southward "advection" by the "bottom advection sheet," leading to strong bottom-trapped ocean currents not present in the traditional flat-bottom ocean.

Figures 2, 3 and 4 depict a numerical solution of (3.3) with $\varepsilon = \kappa = 0.05$, eastern boundary pressure (3.6), and no-normal-flow conditions at all other boundaries. We defer discussion of the numerical method until Section 4. The surface pressure (Fig. 2a) results from the westward "beta advection" and small "diffusion" terms in (3.7). In water shallower than $\frac{1}{2}$, the westward "advection" within the body of the fluid carries the eastern-boundary pressure into the continental slope. There the "bottom advection sheet" "advects" ϕ southward along isobaths, producing the pattern of southward-shifted bottom pressure extrema shown in Figure 2b.

The horizontal velocity at the ocean surface and bottom are shown in Figures 2c and 2d, respectively. The surface velocity (Fig. 2c) is geostrophic except very near the equator, where the pressure gradient in the x-direction drives an eastward jet out of the domain. The bottom velocity (Fig. 2d) is also geostrophic, but its relationship to the pressure field is more complex. We use boundary-layer theory to explain it.

Assume, for simplicity, that $f^2 \gg \varepsilon^2$; this inessential assumption excludes a narrow strip along the equator. Combining the nondimensional equations (3.3) into a single equation for the pressure, we obtain

$$-\frac{\beta}{f^2}\frac{\partial\phi}{\partial x} = \nabla \cdot \left(\frac{\varepsilon}{f^2}\nabla\phi\right) + \frac{\partial}{\partial z}\left(\kappa\frac{\partial\phi}{\partial z}\right). \tag{3.7}$$

The bottom boundary condition is

$$-\kappa\frac{\partial\phi}{\partial z} = \frac{1}{f}J(H,\phi) + \frac{\varepsilon}{f^2}\nabla\phi \cdot \nabla H \qquad \text{at} \qquad z = -H(x). \tag{3.8}$$

Let ε and κ be asymptotically small. Let $\phi_I(x, y, z)$ be the *interior pressure*, the pressure outside the boundary layers near the bottom and vertical sidewalls. Then, by (3.7),

$$\frac{\partial\phi_I}{\partial x} = 0 \tag{3.9}$$

and hence

$$\phi_I(x, y, z) = \phi_E(y, z). \tag{3.10}$$

In general, the interior pressure (3.10) does not satisfy the bottom boundary condition (3.8) with $\varepsilon = \kappa = 0$. Therefore, we expect a bottom boundary layer wherever $\phi_I(x, y, -H(x)) \neq 0$. Within this bottom boundary layer, the balance in (3.7) is between the normal component of the "beta advection" (the left-hand side of (3.7)) and the normal component of the horizontal (ε-) or vertical (κ-) "diffusion" terms on the right-hand side. Suppose that $\kappa \gg \varepsilon$. Then, unless the bottom slope is infinite (vertical sidewall), the boundary layer *correction pressure* $\tilde{\phi}$ obeys

$$-\frac{\beta}{f^2}\frac{\partial\tilde{\phi}}{\partial n}(\mathbf{n} \cdot \mathbf{i}) = \kappa\frac{\partial^2\tilde{\phi}}{\partial n^2}(\mathbf{n} \cdot \mathbf{k})^2, \tag{3.11}$$
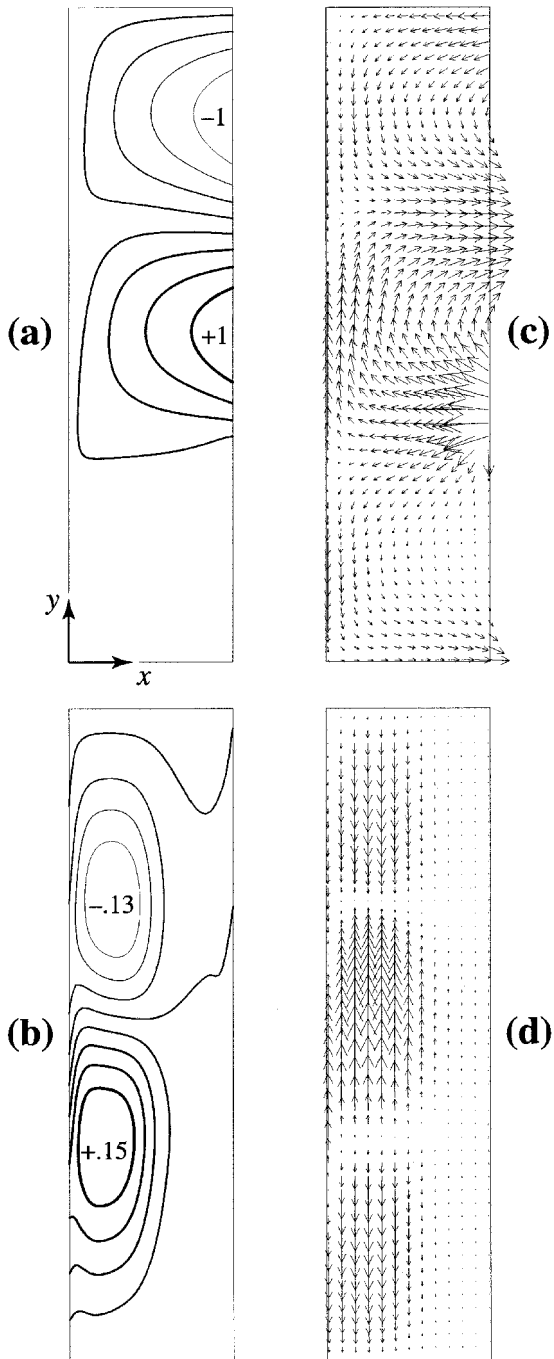
Figure 2 The surface pressure (a), bottom pressure (b), and the horizontal velocity at the surface (c) and bottom (d) in a solution of (3.3) in the western boundary domain (3.4), with $\varepsilon = \kappa = 0.05$. The prescribed pressure (3.6) at the right, open, boundary varies between -1 and $+1$. Darker pressure contours correspond to larger values. The length of the arrows is proportional to the magnitude of the velocity, and the longest arrow corresponds to a (nondimensional) velocity of 35.6.
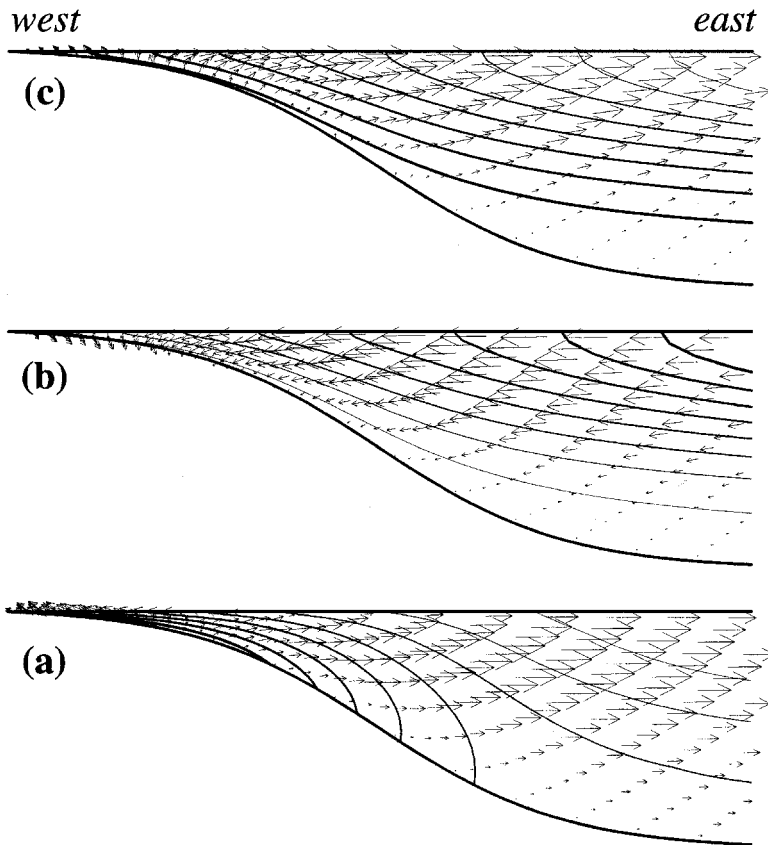
west   **east**

Figure 3. East-west sections of ϕ at (a) $y = \frac{1}{6}$, (b) $y = \frac{1}{2}$, and (c) $y = \frac{5}{6}$ in the same solution as in Figure 2. These latitudes correspond to the three bottom-velocity extrema in Figure 2d. Darker contour lines correspond to larger values of pressure. The arrows represent the velocity tangent to the section.

and the bottom boundary layer has thickness κ. Here,

$$\mathbf{n} = \frac{(H_x, H_y, 1)}{\sqrt{1 + H_x^2 + H_y^2}} \qquad (3.12)$$

is the upward-pointing unit normal to the bottom, and n is the distance from the bottom in the direction of $\mathbf{n}$. The solution

$$\tilde{\phi}(x, y, n) = \tilde{\phi}_b(x, y)e^{-\lambda n}, \qquad \lambda \equiv \frac{\beta}{f^2\kappa} \frac{(\mathbf{n} \cdot \mathbf{i})}{(\mathbf{n} \cdot \mathbf{k})^2}, \qquad (3.13)$$

south   north

(a)

(b)

(c)

(d)
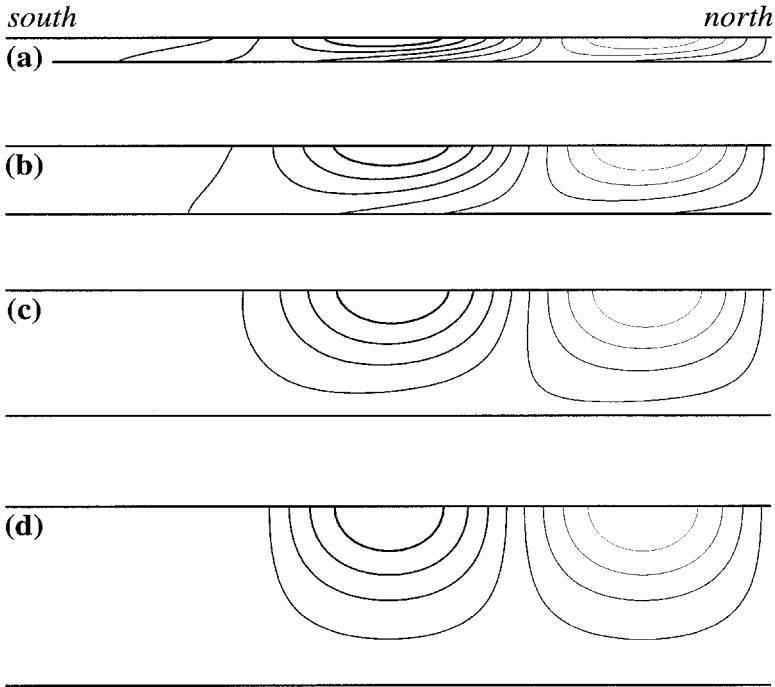
Figure 4. North-south sections of ϕ along the western continental slope at (a) $x = 0.07$, (b) $x = 0.11$, (c) $x = 0.15$, and (d) $x = .25$ in the same solution as in Figures 2 and 3. Thus (d) depicts the eastern-boundary condition (3.6). In the shallower sections (a, b) the pressure near the bottom is skewed toward the south (left) by the "bottom advection sheet."

satisfies (3.11) and decays toward the ocean interior. The boundary layer correction $\tilde{\phi}_b(x, y)$ to the interior bottom pressure $\phi_{Ib}(x, y) \equiv \phi_I(x, y, -H(x, y))$ is determined by the bottom boundary condition (3.8), in the form

$$-\kappa \left[\frac{\partial \tilde{\phi}}{\partial n}\right]_b (\mathbf{n} \cdot \mathbf{k}) = \frac{1}{f} J(H, \phi_b) = \frac{1}{f} J(H, \phi_{Ib} + \tilde{\phi}_b), \tag{3.14}$$

(still assuming $\kappa \gg \varepsilon$). That is,

$$\kappa \lambda (\mathbf{n} \cdot \mathbf{k}) \tilde{\phi}_b = \frac{1}{f} J(H, \phi_b). \tag{3.15}$$

We regard (3.15) as an advection-decay equation for $\phi_b(x, y)$ in the form

$$J(-H, \phi_b) = -f \kappa \lambda (\mathbf{n} \cdot \mathbf{k})(\phi_b - \phi_{Ib}), \tag{3.16}$$

where $f \kappa \lambda (\mathbf{n} \cdot \mathbf{k})$ is the "decay coefficient" and $-H$ is the "streamfunction" for the "flow"

"advecting" $\phi_b(x, y)$. Equivalently,

$$\frac{d\phi_b}{ds} = -\mu(\phi_b - \phi_{Ib}), \tag{3.17}$$

where

$$\mu \equiv \frac{f\kappa\lambda(\mathbf{n} \cdot \mathbf{k})}{|\nabla H|} = \frac{\beta}{f} \frac{(\mathbf{n} \cdot \mathbf{i})}{|\nabla H| (\mathbf{n} \cdot \mathbf{k})} = \frac{\beta}{f} \frac{H_x}{|\nabla H|}, \tag{3.18}$$

and s is the distance measured along isobaths, with deep water on the left, that is, southward on the western continental slope. Thus, as anticipated by the discussion in Section 2, the bottom pressure is "advected" southward along isobaths, while decaying toward the local interior bottom pressure. If $H_y = 0$, the decay distance μ^{-1} is f/β, the planetary radius. If, for example, the continental slope extends infinitely in the y-direction, then the solution of (3.17) is

$$\phi_b(x, y) = \frac{\beta}{f} \int_y^\infty \phi_I(x, y', -H) e^{\beta/f(y-y')} dy' \tag{3.19}$$

(approximately, because (3.19) treats β/f as a constant). Thus the bottom pressure is an average of the interior pressure at the bottom, northward along the same isobath, over a distance equal to the planetary radius. This explains the southward shift of the bottom pressure in Figure 2b.

If $\varepsilon \gg \kappa$, then friction balances "beta advection" in a bottom boundary layer of thickness ε, but the analysis is very similar to that presented above, and in fact (3.19) is unchanged. However, since we eventually consider the limit $\kappa \to \infty$, we shall continue to assume that κ dominates ε.

To understand the bottom velocity in Figure 2d, we look more closely at the boundary layer solution (3.13). According to (3.13) and (3.17–18), the boundary layer correction pressure $\tilde{\phi}$ has the same magnitude as the interior pressure ϕ_I. However, $\tilde{\phi}$ decays rapidly in the direction normal to the bottom; the decay distance is $O(\kappa)$. Therefore, the correction pressure makes a dominant, $O(\kappa^{-1})$, contribution to $\partial\phi/\partial x$ near the bottom. However, the contribution of $\tilde{\phi}$ to $\partial\phi/\partial y$ is only $O(1)$, the same size as the contribution from ϕ_I. It follows that the northward velocity

$$v = \frac{1}{f} \frac{\partial\phi}{\partial x} - \frac{\varepsilon}{f^2} \frac{\partial\phi}{\partial y} \tag{3.20}$$

in the bottom boundary layer is $O(\kappa^{-1})$ and negatively proportional to $\tilde{\phi}_b(x, y)$. That is, a positive bottom-boundary-layer correction pressure corresponds to a large negative $\partial\phi/\partial x$, because the bottom slopes downward to the east, and because the boundary-layer

correction pressure decays toward the interior. On the other hand, the eastward velocity

$$u = -\frac{1}{f}\frac{\partial \phi}{\partial y} - \frac{\varepsilon}{f^2}\frac{\partial \phi}{\partial x} \tag{3.21}$$

is O(1) and is not simply related to $\tilde{\phi}_b(x, y)$. Therefore, the horizontal velocity on the sloping bottom is directed along isobaths, and is generally stronger than the velocity at the surface, in agreement with Figure 2. The most *positive* $\tilde{\phi}_b$ occurs on the southern third of the continental slope (just south of the most positive ϕ_I); there the northward velocity must be *negative,* in agreement with Figure 2d. The same type of reasoning explains the other velocity extrema in Figure 2d. The bottom pressure depicted in Figure 2b includes both the interior pressure and the boundary-layer correction pressure. Thus the bottom pressure is *not* simply related to the horizontal velocity (Fig. 2d) at the bottom.

Figure 3 shows east-west sections of ϕ at the three latitudes ($y = \frac{1}{6}, \frac{1}{2}, \frac{5}{6}$) of maximum bottom velocity. The arrows represent the velocity tangent to the sections. As expected, the cross-shore velocity is about 20 times smaller than the longshore bottom velocity in Figure 2d. By (3.3c, d), the vertical velocity is negatively proportional to $\partial \phi / \partial z$.

Figure 4 shows south-north sections of ϕ at $x = 0.07, 0.11, 0.15, 0.25$. The longitude $x = 0.07$ (Fig. 4a) coincides with the bottom-pressure extrema in Figure 2b. The longitude $x = 0.11$ (Fig. 4b) coincides with the bottom-velocity extrema in Figure 2d. Figure 4d depicts the "inflow" boundary condition (3.6). In both Figures 3 and 4, the bottom boundary layer is visible as a bunching and southward shifting of the pressure contours near the bottom. This bunching is slight because the nondimensional decay parameters are still relatively large ($\varepsilon = \kappa = 0.05$). In the following section, we consider solutions with much smaller values of these decay parameters, in which the asymptotic character of the boundary layers is more evident. In the remainder of this section, we consider solutions with large values of κ, in order to investigate the transition to the homogeneous-fluid limit.

The limit of homogeneous fluid corresponds to $\kappa \to \infty$. In the limit $\kappa \to \infty$, ϕ is z-independent at leading order, and is determined by

$$J\left(\phi, \frac{H}{\hat{f}}\right) = \nabla \cdot \left(\frac{\varepsilon H}{f^2 + \varepsilon^2}\nabla \phi\right) + \int_{-H}^0 W\, dz. \tag{3.22}$$

In the limit of homogeneous fluid, (2.30) reduces to the equation (2.32) discussed in Section 2. Eqs. (3.22) and (2.32) are physically equivalent, and equally easy to interpret as "advection-diffusion" equations, but the simpler boundary condition ($\psi = 0$) on ψ has led to a preference for (2.32).

Figures 5 and 6 show numerical solutions of (3.3) in the domain (3.4–5) with $\kappa = 10$ and 100, respectively. These solutions have the same small value of $\varepsilon = 0.05$ as the solution
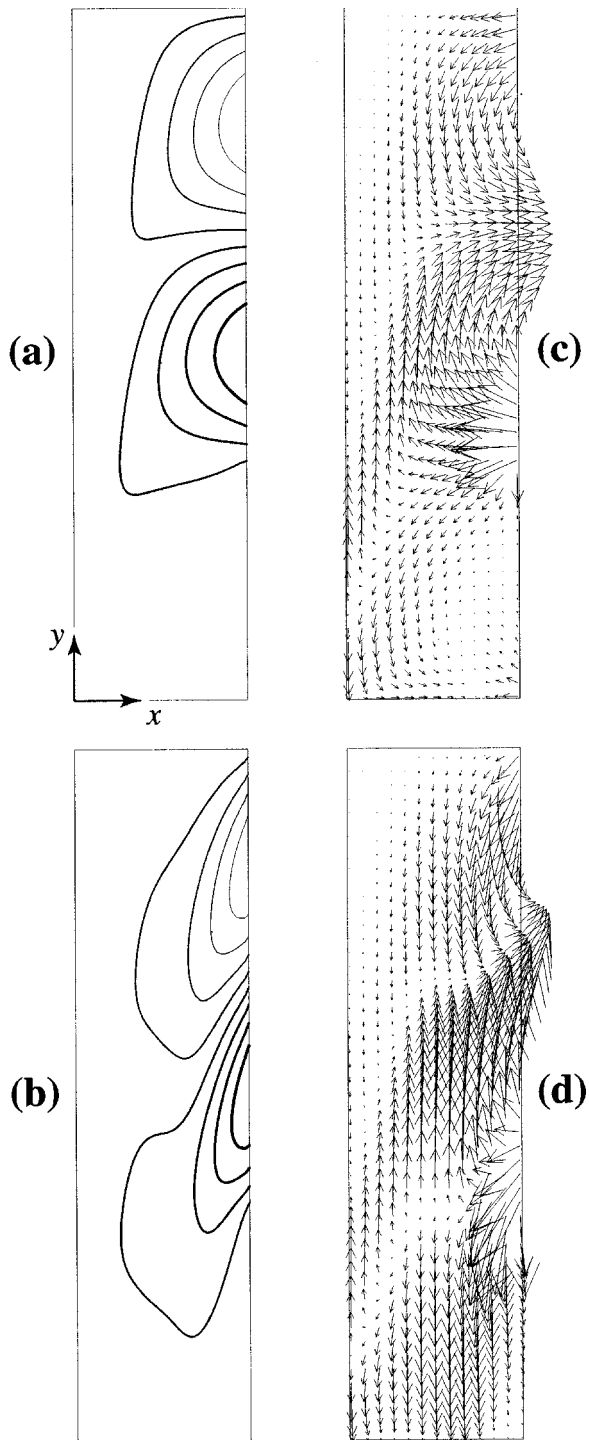
Figure 5. The same as Figure 2, but with a larger $\kappa = 10$ and the z-independent open-boundary condition (3.23). The flow has begun to resemble the depth-independent flow depicted in Figure 1d for the case of homogeneous fluid, which corresponds to the limit $\kappa \to \infty$ in (3.3).
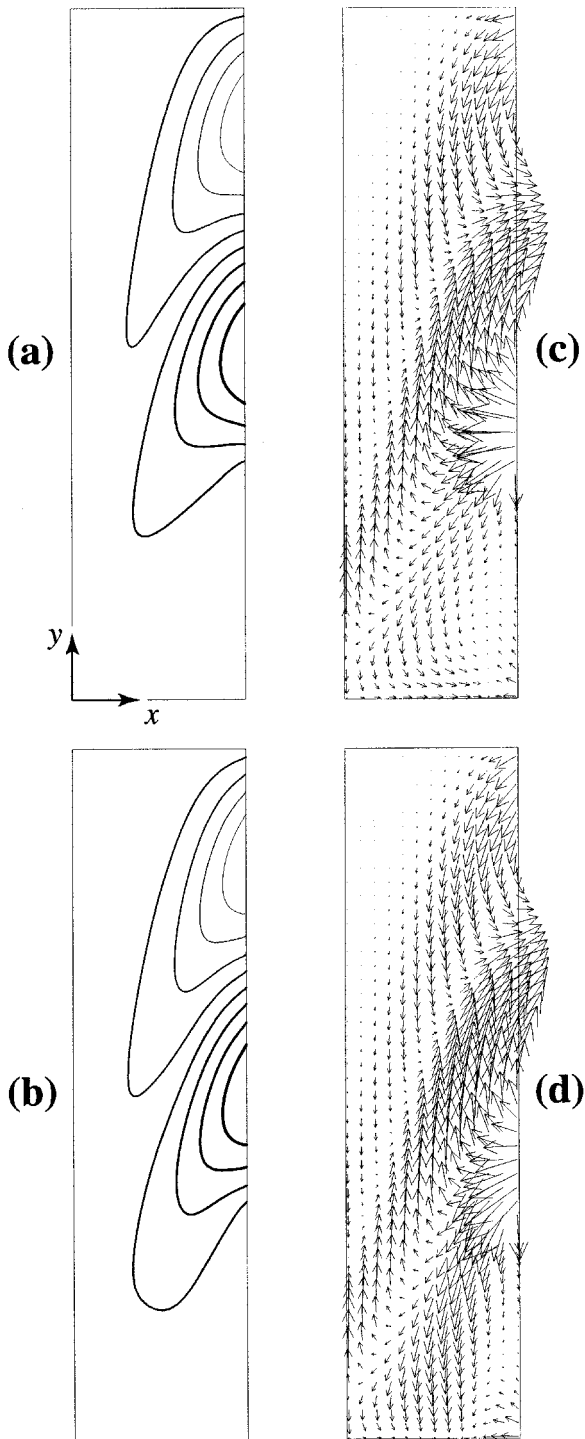
Figure 6. The same as Figure 5, but with a still larger $\kappa = 100$. Now the flow closely resembles the homogeneous fluid limit ($\kappa \to \infty$).

shown in Figures 2–4. However, at these large values of κ, it is sensible to prescribe an open-boundary pressure $\phi_E(y, z)$ that is z-independent. We therefore choose

$$\phi_E(y) = \begin{cases} 0, & 0 < y < \frac{1}{3} \\ -0.441 \sin(3\pi(y - \frac{2}{3})), & \frac{1}{3} < y < 1 \end{cases} \tag{3.23}$$

which has the same vertical average as (3.6). For $\kappa = 10$ (Fig. 5), the top and bottom pressures differ significantly, and ϕ is still far from the state of z-independence corresponding to $\kappa \to \infty$. In fact, even for $\kappa = 100$ (Fig. 6), we see differences between the pressures at the top and bottom, and the horizontal flow at the bottom is still slightly stronger than at the surface. However, the pressure in Figure 6 closely resembles the homogeneous-fluid solution shown in Figure 1d.

Comparing Figures 2, 5 and 6, we see that, as κ increases, the three regions of strong bottom velocity observed in Figure 2d move offshore, thicken, and interleave to form the pattern observed in Figure 1d.

4. North Atlantic solutions

In this section and the next, we examine solutions of the linear dynamical equations (2.1) with realistic North Atlantic bathymetry and observed wind stress. In the case of realistic bathymetry, it is best to work in dimensional variables and spherical coordinates. In spherical coordinates, the integral (2.20) takes the dimensional form

$$I[\phi, \alpha] = \iiint d\lambda \, d\mu \, dz \left\{ \frac{f}{f^2 + \varepsilon^2} \frac{\partial(\phi, \alpha, z)}{\partial(\lambda, \mu, z)} - \frac{\varepsilon}{f^2 + \varepsilon^2} \right.$$
$$\cdot \left(\frac{1}{\cos\mu} \frac{\partial\phi}{\partial\lambda} \frac{\partial\alpha}{\partial\lambda} + \cos\mu \frac{\partial\phi}{\partial\mu} \frac{\partial\alpha}{\partial\mu} \right) \tag{4.1}$$
$$\left. - r_e^2 \cos\mu \frac{k}{N^2} \frac{\partial\phi}{\partial z} \frac{\partial\alpha}{\partial z} + r_e \left(u^\tau \frac{\partial\alpha}{\partial\lambda} + \cos\mu \, v^\tau \frac{\partial\alpha}{\partial\mu} \right) \right\}$$

where (λ, μ) is the (longitude, latitude), (u, v) is the horizontal velocity in the (east, north) direction, and r_e is the radius of the Earth. The spherical-coordinate version of (2.5) and the no-normal-flow boundary conditions result from the requirement that $\delta (4.1)/\delta\alpha = 0$.

We partition the whole ocean into hexahedral finite elements whose sides conform to the coastlines and to the top and bottom boundaries, as shown in Figures 13 and 19. Within each element, the pressure $\phi(\lambda, \mu, z)$ and test function $\alpha(\lambda, \mu, z)$ vary continuously with location, in a manner determined solely by their respective values at the 8 nodes (i.e. corners) of the element. Hence the numerical approximation to (4.1) is an ordinary function of all the nodal values of ϕ and α. The numerical analogue of (2.5) is just the derivative of this function with respect to each interior nodal value of α. The numerical analogue of the no-normal-flow boundary condition is just the derivative with respect to those values of α

corresponding to nodes on the top or bottom boundaries. For further details of the numerical method, refer to the Appendix.

In all of the solutions discussed, the horizontal resolution is 0.25° in latitude and longitude, that is, about 25 km. As explained in the Appendix, the vertical resolution depends on vertical location and on the ocean depth. In water 4 km deep, only 50 m separates the two nodes nearest the top and bottom, but the nodal separation increases to 360 m in midwater. In shallower water, the vertical resolution is greater at the corresponding depths; see Figure 19 (top). The relatively high vertical resolution near the top and bottom of the ocean is needed to resolve the prescribed Ekman layer and the bottom boundary layer.

The bathymetry (Fig. 7) is smoothed ETOPO5 data at 15 min spacing. At this resolution and depth, only the islands of Cuba, Hispaniola, Newfoundland and Ireland are resolved; shoals represent the other islands. To reduce and close the computational domain, coasts were created in the shallow regions of the St Lawrence Gulf, Hudson Strait, Davis Strait, Iceland-Faroe Ridge, North Sea, and Gibraltar. The Gulf of Guinea was removed. A rigid vertical wall lies along the equator, corresponding to the boundary condition of cross-equatorial symmetry.

For the wind forcing, we take

$$\tau(\lambda, \mu, z) = \tau_s(\lambda, \mu) \exp(z/\delta_E) \qquad (4.2)$$

where τ_s is the annually averaged wind stress of Hellerman and Rosenstein (1983), and δ_E is the prescribed "Ekman layer" depth. In all the solutions discussed, $\delta_E = 100$ m. Near the equator, and especially in the eastern Atlantic, the wind stress was modified to be compatible with the imposed boundary condition of cross-equatorial symmetry in the flow. (Of course, the wind stress is arbitrary, but wind stress incompatible with no normal flow across the equator would lead to prominent artificial frictional boundary layers at the equator.) The wind forcing (4.2) determines the "source term"

$$W(\mu, \lambda, z) = W_s(\mu, \lambda) \exp(z/\delta_E) \qquad (4.3)$$

in the ϕ-equation (2.5). Figure 8 shows the corresponding field of $f\delta_E W_s$, where $W_s = W(\lambda, \mu, 0)$. Away from the equator, $f\delta_E W_s \approx -\operatorname{curl} \tau_s$. Note the strong positive "source" of ϕ in the eastern Caribbean.

The remaining parameters of the model are the decay coefficients ε and k, and the Vaisala frequency $N(z)$. The latter two enter the physics only in the ratio k/N^2. It is tempting to choose $N(z)$ to resemble the observed horizontal average, and many solutions (not shown in this paper) were computed with a prescribed $N(z)$ that decayed exponentially with depth and resembled the horizontally averaged North Atlantic stratification. However, the observed stratification varies significantly with horizontal location. In particular, the observed main thermocline thickness increases greatly from east to west. Hence, the prescription of an $N(z)$ with vertical (but no horizontal) variation cannot make the solutions
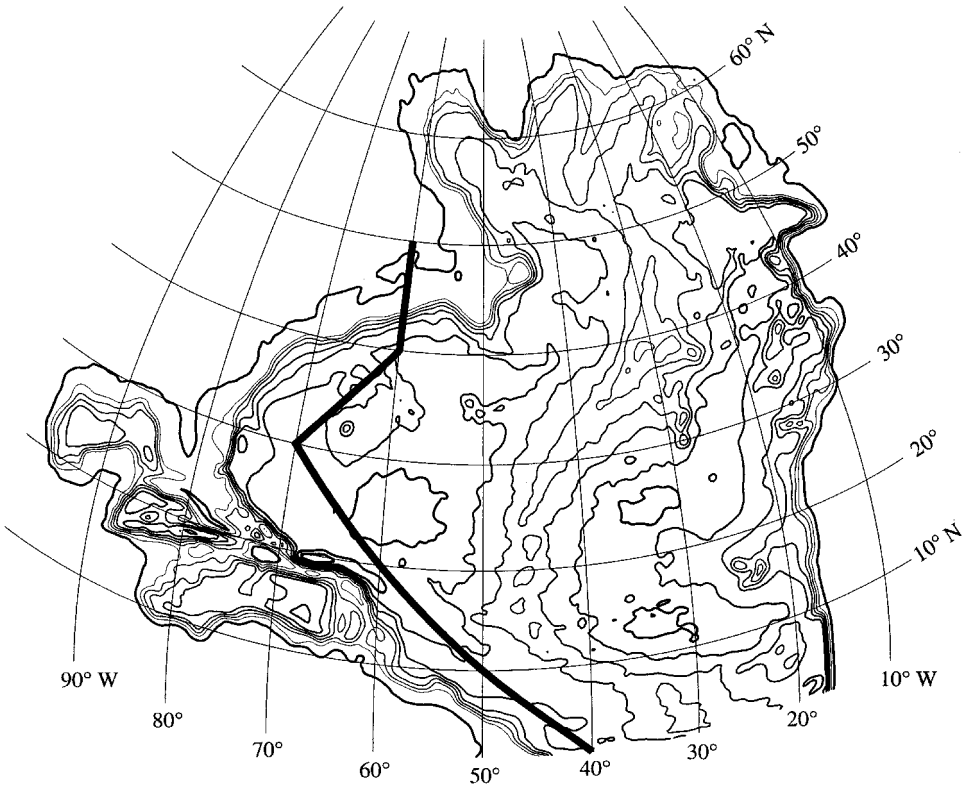
Figure 7. Bathymetry for the North Atlantic solutions. Contour interval, 825 m. Darker contours correspond to greater depths. The only resolved islands are Cuba, Hispaniola, Newfoundland and Ireland. In the *full basin* (FB) solution introduced in Section 4, we solve the linear dynamics over the entire region depicted. In the *western windless* (WW) solutions discussed in Section 5, we neglect the wind forcing *W* in the region west of the heavy line, and use the FB result as an open boundary condition on the heavy line.

more realistic. We prefer to let the model predict the *entire* variation in the stratification, and hence we choose N to be a constant. Thus we are linearizing about a rest state with a uniform stratification. However, the value of N is actually *irrelevant,* because a change in N^2 is undetectable from a change in k. Once again, the parameters k and N^2 enter the model only in the ratio k/N^2.

On these assumptions, the only parameters of the model are the constants ε and k/N^2 (but see the Appendix for discussion of an additional parameter, the fraction, s, of upwind differencing added for numerical stability). The parameter k/N^2 controls the thermocline thickness (3.2). For

$$\frac{k}{N^2} = 1.0 \times 10^{-9} \text{ day} \tag{4.4}$$
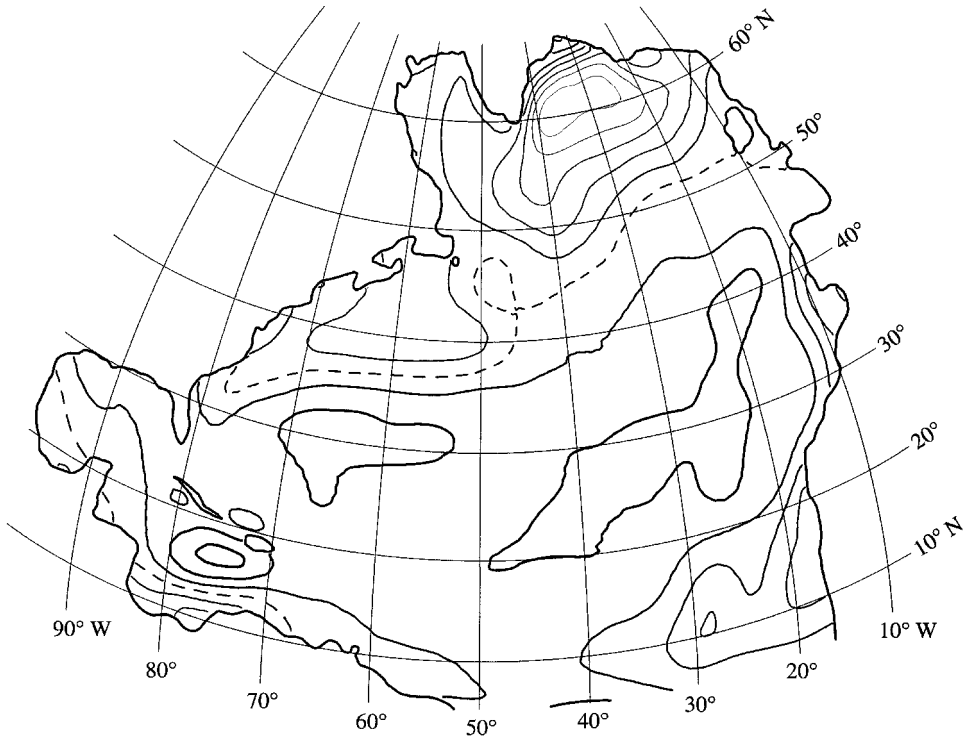
Figure 8. The quantity $f\delta_E W_s$, which, away from the equator, approximately equals *minus* the wind stress curl. W_s is the surface value of the "source term" W in the ϕ-equation (2.5). Darker contours correspond to larger values of W_s, and the zero contour is dashed. Contour interval, 4.0×10^{-5} km day^{-2} (equivalent to 5.2×10^{-10} cgs). Note the large positive source in the eastern Caribbean.

and an ocean width of, say, 6000 km, (3.2) with (4.4) predicts a thermocline thickness of about 500 m near the western boundary. All the solutions discussed use the value (4.4).

This leaves ε as the single undetermined parameter of the model, and the only model parameter not tightly constrained by observations. In a homogeneous ocean with a flat bottom, the western boundary layer thickness is ε/β. However, this fact has little relevance to the stratified case with topography. If ε dominates k, then (by an elementary analysis, or virtually by inspection of (2.5)) the bottom boundary layer thickness is

$$\delta_\varepsilon = \frac{\varepsilon}{\beta} \frac{S}{\sqrt{1+S^2}} \tag{4.5}$$

where S is the bottom slope. In the limit of a vertical wall ($S \to \infty$), ε always dominates, and $\delta_\varepsilon \to \varepsilon/\beta$. If, on the other hand, k dominates ε, then the bottom boundary layer thickness is

$$\delta_k = \frac{k}{N^2} \frac{f^2}{\beta} \frac{1}{S\sqrt{1+S^2}}. \tag{4.6}$$
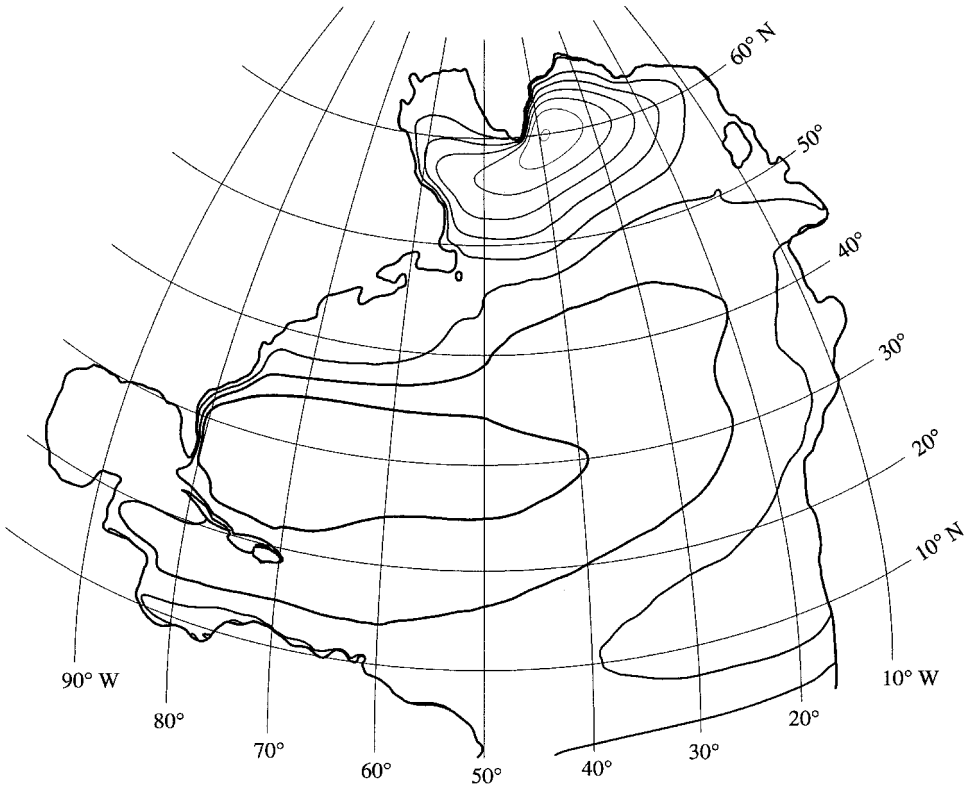
Figure 9. The sea-surface elevation in the full-basin solution FB with the observed time-average wind stress and friction parameter $\varepsilon/\beta = 25$ km. Darker contours correspond to larger elevations. Contour interval, 13.3 cm. Range, 119.0 cm.

The condition for ε to dominate k is $\delta_\varepsilon > \delta_k$. Hence, with (4.4), ε dominates k at midlatitude if

$$\frac{\varepsilon}{\beta} > \frac{4.0 \times 10^{-2} \text{ m}}{S^2}. \tag{4.7}$$

In the model ocean basin used in our calculations (Fig. 7), the maximum bottom slope is about $S = 10^{-2}$, for which (4.7) takes the value 400 m.

In most of the solutions discussed, $\varepsilon/\beta = 25$ km, corresponding to a flat-bottom western boundary layer thickness of 25 km, which approximately equals the horizontal spacing between nodes. According to (4.7) with $\varepsilon/\beta = 25$ km, ε dominates k at all slopes greater than $S = 10^{-3}$. For $S = 10^{-3}$, the bottom boundary layer thickness (4.5) is 25 m. In the following section, we also examine a solution with a much smaller $\varepsilon/\beta = 1$ km.

Figures 9–11 show a solution (solution FB, for *full basin*) with friction parameter $\varepsilon/\beta = 25$ km, and the wind forcing of Figure 8. The sea surface (Fig. 9) slopes most steeply near
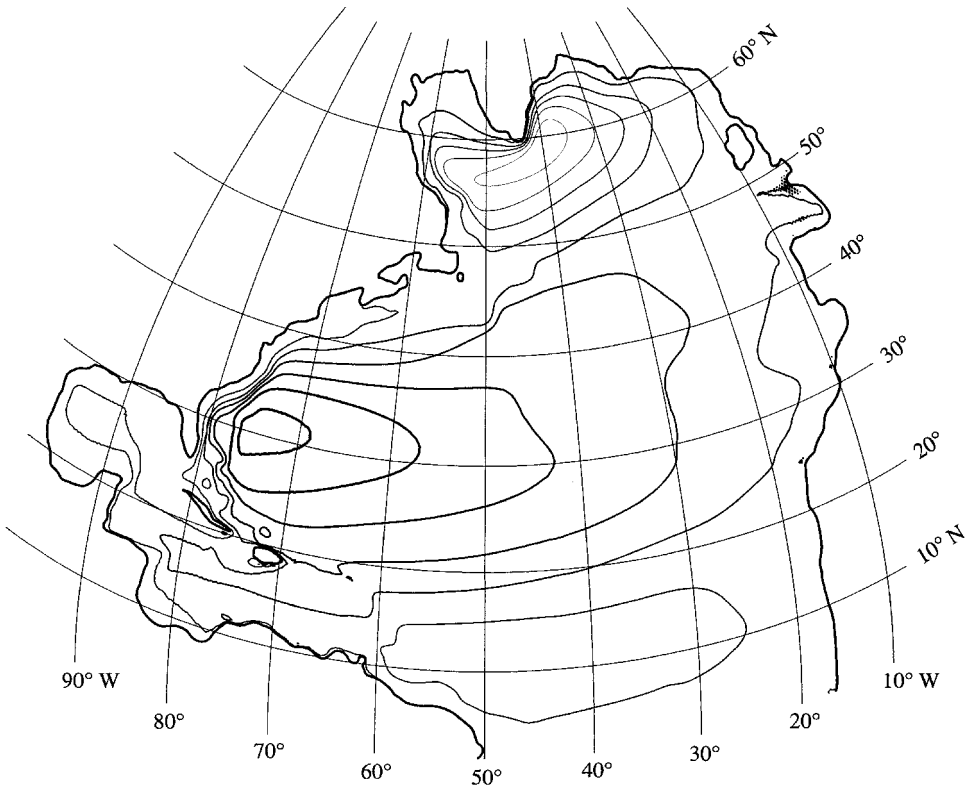
Figure 10. The streamfunction for the vertically integrated flow in the same solution (FB) as Figure 9. Darker contours correspond to larger values of streamfunction. Contour interval, 5.54 Sverdrups. Range, 49.9 Sverdrups.

the western boundary, where the surface velocity is greatest, but Figure 10 shows that the maximum transport occurs in the deeper water above the continental slope. The transport through the Caribbean and, particularly, through the Gulf of Mexico, is unrealistically small. We shall argue that this is an inevitable consequence of linear theory. However, in a synthesis of North Atlantic observations, Schmitz and McCartney (1993) propose that, of the 30 Sv (1 Sv = 1 Sverdrup = 10^6 m^3 sec^{-1}) passing through the Straits of Florida, only about 17 Sv represents water circulating through the subtropical gyre, and that most of this 17 Sv passes east of 60W. The remaining 13 Sv represents warm, low-salinity water crossing the equator along the South American shelf. In the solution described here, this cross-equatorial source is prevented by the equatorial boundary condition of no-normal-flow. Figure 10 does indeed show the 17 Sv originating east of 60W, but virtually none of that 17 Sv passes between Florida and Cuba. A significant portion enters the Caribbean, but most of this flow exits again, through the Windward and Mona Passages, to flow northward east of the Bahamas. Thus, in linear theory, even the transport recirculating in the subtropical gyre does not pass between Cuba and Florida.

In the remainder of this paper, we focus on the region of strong currents and complex bathymetry in the western subtropical North Atlantic. Despite the unrealistic Caribbean flow, this western region of large bottom pressure and irregular, steep bathymetry is the ideal region in which to study the interaction between linear dynamics and ocean bottom topography of realistic complexity. Once again, our purpose is not to inflate or defend linear theory, but to understand its results as completely as possible.

5. The western region

In this section we concentrate on the region west of 70W. Figure 12 shows the bathymetry of this complex region, with different contour intervals above and below 1000 m depth. Once again, Cuba and Hispaniola are the only resolved islands. Figure 13, a closeup of the region around Florida and Cuba, shows how the finite elements conform to the coastlines.

In the usual flat-bottom linear theory, the wind forcing inside the western boundary layer is negligible compared to the large frictional and beta terms there. However, in our solutions, western bottom boundary layers are present throughout the Caribbean and Gulf of Mexico, and there is no single narrow region of strong flow. Still, we try to understand the flow in the western North Atlantic by neglecting the wind forcing in the region west of the heavy line in Figure 7. In these *windless western* (hereafter WW) solutions, we solve the ϕ-equation (2.5) or (2.11) in this western region with the ''source'' term W removed, using the ϕ-values computed in the wind-driven, full-basin solution FB described in Section 4 as the boundary condition at the open boundary, that is, along the heavy line in Figure 7. This open-boundary condition drives the flow inside the western region. Since W vanishes inside the western region, our interpretation of the WW solutions relies only on the ''advection'' and ''diffusion'' of ϕ. Table 1 summarizes all the solutions discussed.

Although the WW solutions are significantly weaker than the FB solution in the western region, WW and FB resemble one another enough to make the simplification worthwhile. However, even the WW solutions are somewhat difficult to interpret, because ''beta advection'' and ''bathymetric advection'' juxtapose ϕ-values from widely separated points on the open boundary. Therefore, we begin by examining a WW solution with a highly localized open-boundary condition. In this idealized solution, we take

$$\phi(\mu, z) = 100 \text{ cm} \times \exp\left\{-\frac{(\mu - 30\text{N})^2}{(1°)^2} - \left|\frac{z}{500 \text{ m}}\right|^2\right\} \tag{5.1}$$

as the pressure on the open boundary. The boundary condition (5.1) corresponds to a near-delta-function source, with half-width of one degree in latitude and 500 m in height, centered at 30N and the ocean surface. The latitude of (5.1) corresponds to the latitude of maximum interior surface pressure in FB—the center of the subtropical gyre. We regard the response to (5.1) as an (approximate) Green's function for the open-boundary problem.
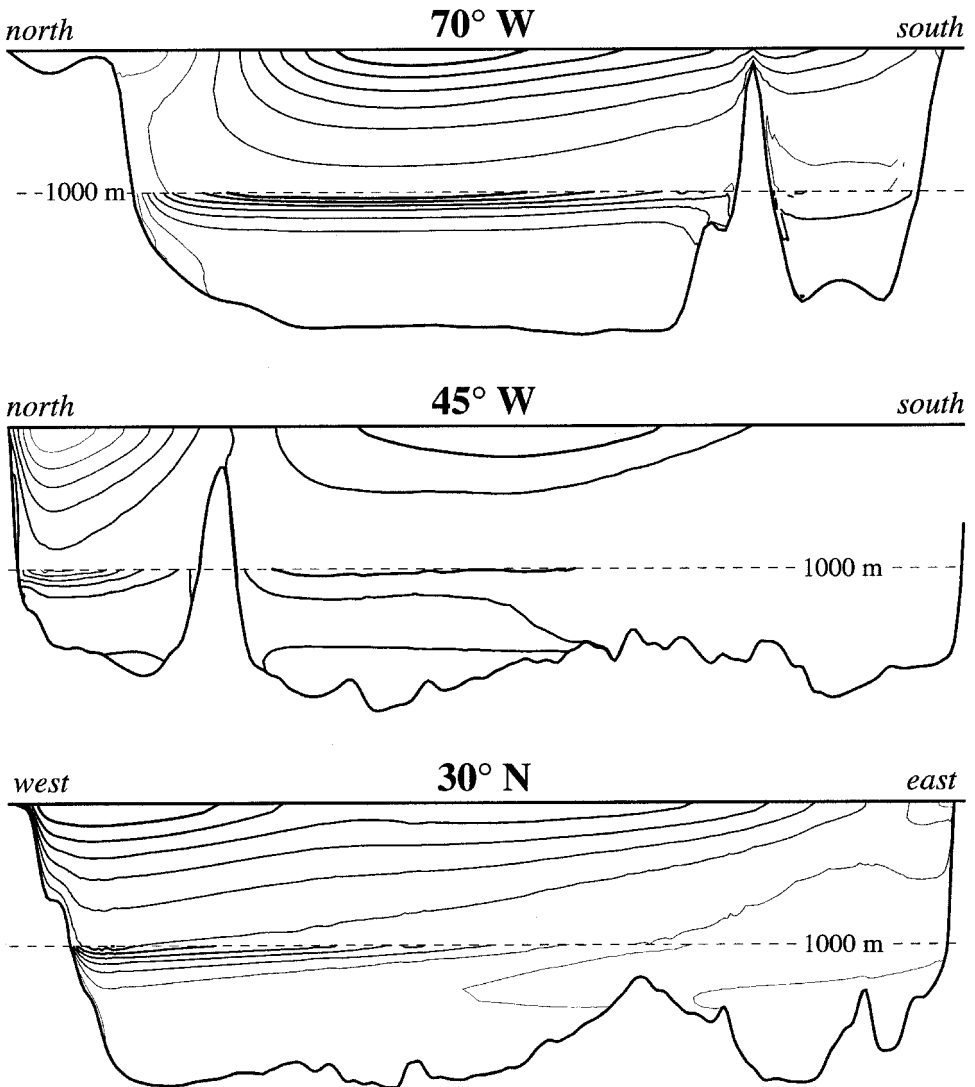
Figure 11. Three sections of pressure ϕ in the same solution (FB) as Figures 9 and 10. On each section, the regions above and below 1000 m depth have different vertical scales and contour intervals. In each region, darker contours correspond to larger ϕ. Bottom: a section along 30N from Florida to Africa. Counter intervals (in units of dynamic centimeters), 4.7 cm above 1000 m and 0.85 cm below 1000 m. Middle: a section along 45W from the tip of Greenland to the Brazilian shelf, contour intervals 10.3 cm and 1.25 cm. Top: a section along 70W from Maine to Venezuela, contour intervals 5.34 cm and 0.63 cm.

Of course, the complete interpretation in terms of Green's functions would involve exact delta functions at every open-boundary latitude and depth, followed by a horrendous superposition of solutions. However, we shall see that some of the most important features of our solutions are understandable from the response to (5.1).
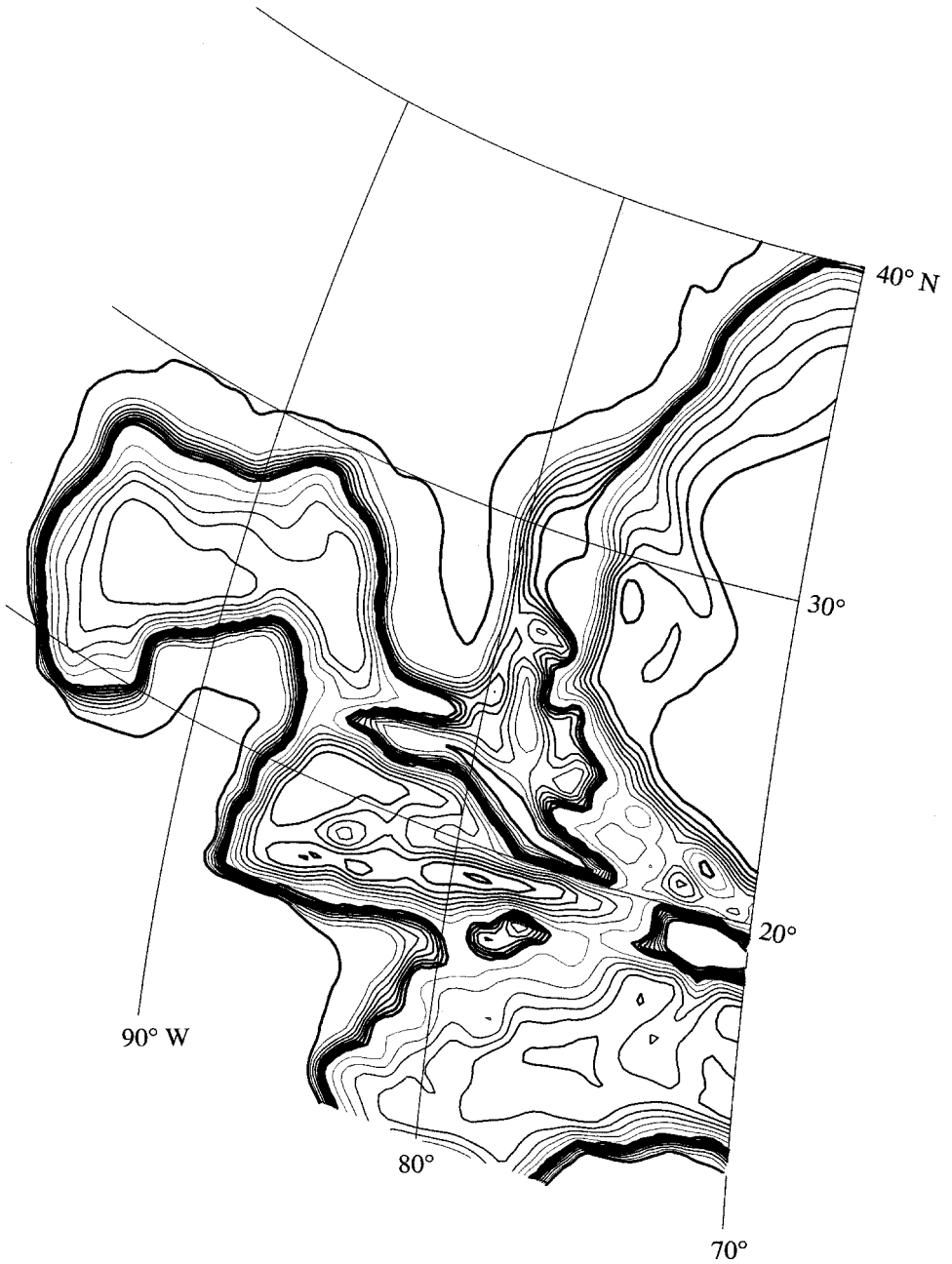
Figure 12. Bathymetry in the region west of 70W. The subregions with ocean depth less than 1000 m and greater than 1000 m are contoured separately. Darker contour lines correspond to greater ocean depth within each of these subregions. Contour intervals: 111 m in the shallower subregion, and 504 m in the deeper subregion. Maximum depth, 5535 m.
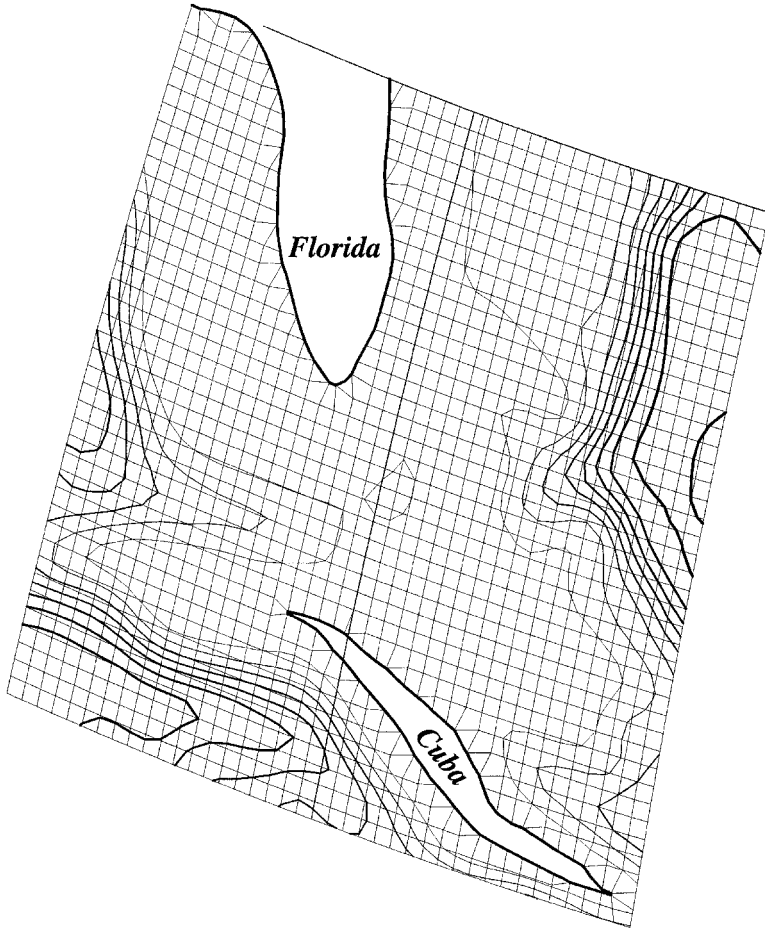
Figure 13. The area around Florida and Cuba, showing how the finite elements conform to the coastline. Depth contour interval, 580 m.

Figures 14–18 show a windless western solution, WWG25, with Green's function boundary condition (5.1), and friction parameter $\varepsilon/\beta = 25$ km. (Although the WW solutions are computed in the entire region west of the heavy line in Figure 7, the figures show only the subregion west of 70W and south of 40N.) In Figure 14, "beta advection"

Table 1. North Atlantic solutions.

	Domain	Wind forcing	Open-boundary condition	ε/β	Figures
FB	full basin	yes	not applicable	25 km	9–11, 23, 24, 28
WW25	western region	no	ϕ from FB	25 km	20, 25, 27
WW1	western region	no	ϕ from FB	1 km	21, 26
WWG25	western region	no	(5.1)	25 km	14–19
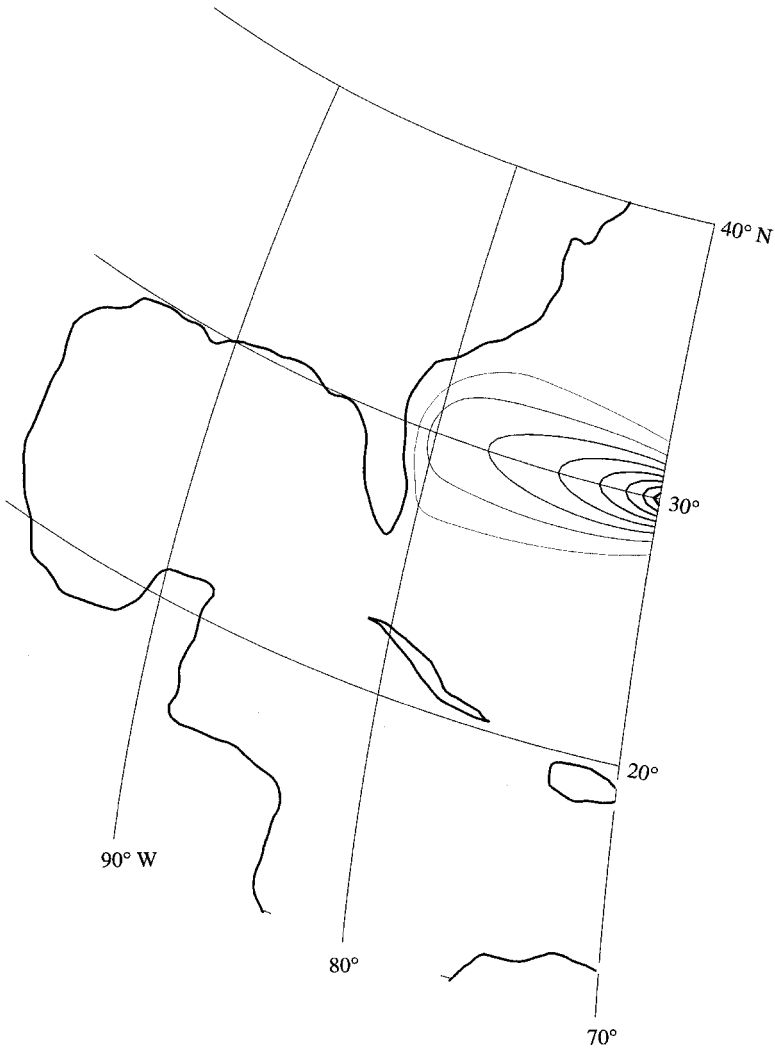
Figure 14. The sea-surface elevation west of 70W in solution WWG25, with Green's function boundary condition (5.1), no local wind forcing, and $\varepsilon/\beta = 25$ km. Contour interval, 11.2 cm. "Beta advection" carries the high surface pressure directly westward to the North American coast.

carries the surface pressure directly westward in a narrow beam. However, the bottom pressure (Fig. 16) shows the strong influence of the "bottom advection sheet," which carries ϕ southward along the isobaths, through the Florida Straits, and counter-clockwise around the Gulf of Mexico. In fact, the tongue of high bottom pressure that begins just east of Miami (from "beta advection" into the continental slope north of the Bahamas) is visible in Figure 16 all the way around to the (submerged) island of Jamaica, on the southern rim of the Cayman trench (the very deep trench south of Cuba).

Figures 15 and 17 show the horizontal velocity at the ocean surface and bottom,
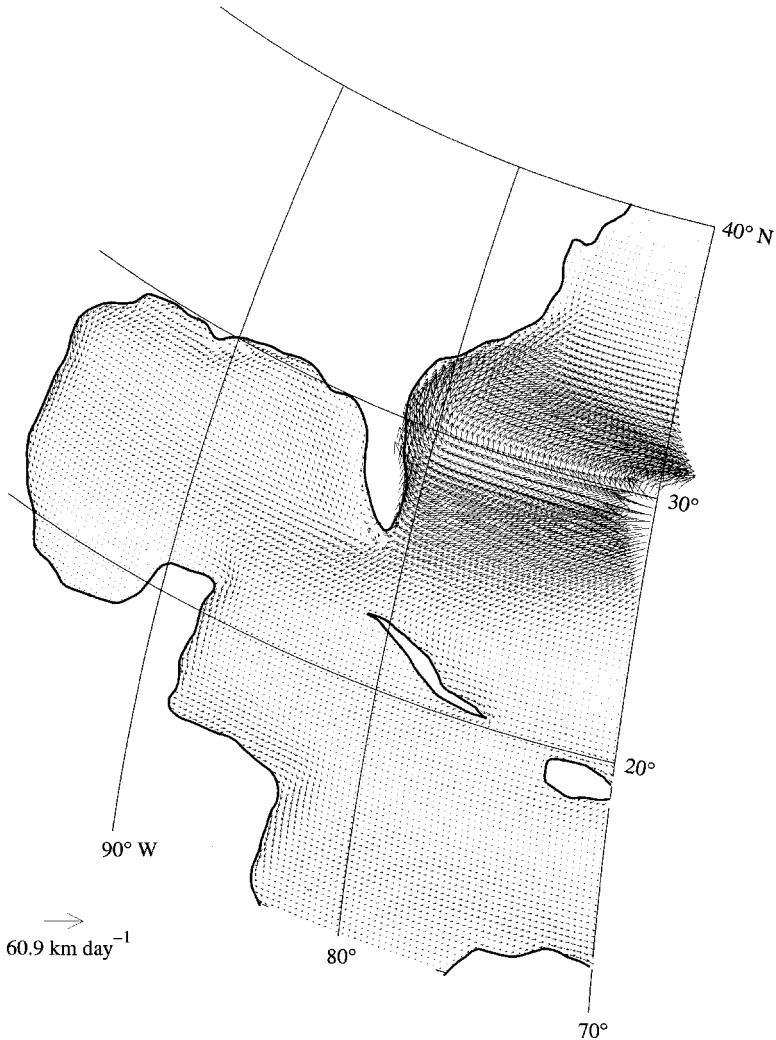
Figure 15. The horizontal velocity at the ocean surface in the same solution (WWG25) as Figure 14. The arrows are proportional to the *square root* of the fluid speed. The longest arrow on the diagram (which has the same size as the arrow at the lower left) corresponds to the maximum velocity of 60.9 km day^{-1}.

respectively. In Figures 15 and 17, and in all other arrow diagrams of velocity, the length of each arrow is proportional to the *square root* of the fluid speed, to minimize the range of arrow sizes. The longest arrow in Figure 17 corresponds to the maximum bottom velocity of 90.7 km day^{-1}, a value 50% greater than the maximum surface velocity in Figure 15. (The longest arrows are reproduced at the bottom left of each arrow figure, and have the same length in every figure. Their corresponding velocity thus sets the scale for the figure.)
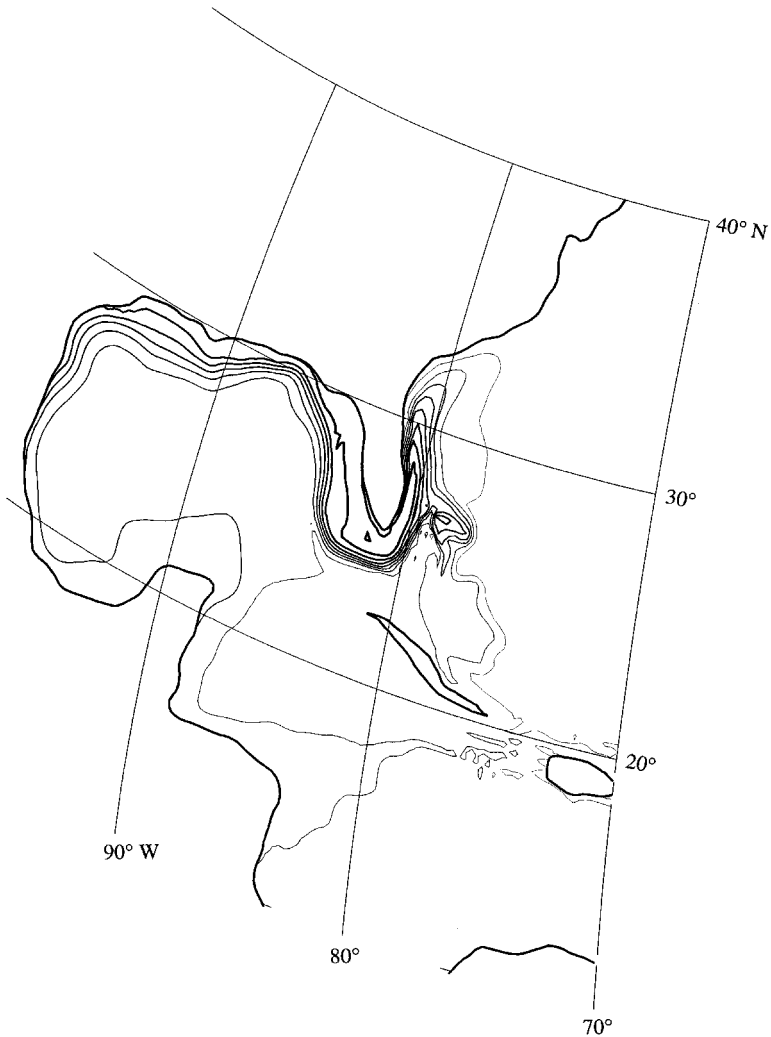
Figure 16. The pressure at the ocean bottom in the same solution (WWG25) as Figures 14 and 15. Darker contours correspond to larger values. Contour interval, 0.43 cm. "Beta advection" carries the high imposed interior pressure at 30N westward into the continental slope, creating the maximum in bottom pressure just east of Florida. Then the "bottom advection sheet" carries the pressure pseudosouthward along isobaths, around the tip of Florida and counterclockwise around the perimeter of the Gulf of Mexico.

According to Figure 17, the largest bottom velocities in WWG25 occur in the coastal region directly west of the source (5.1). Here low values of ϕ, which have been "advected" southward along the bottom, lie very close to the high values of ϕ that have been "beta advected" through the body of the fluid, directly westward from the source. The result is a very large value of $\partial\phi/\partial\lambda$ (where λ is the longitude) near the coast, and a correspondingly
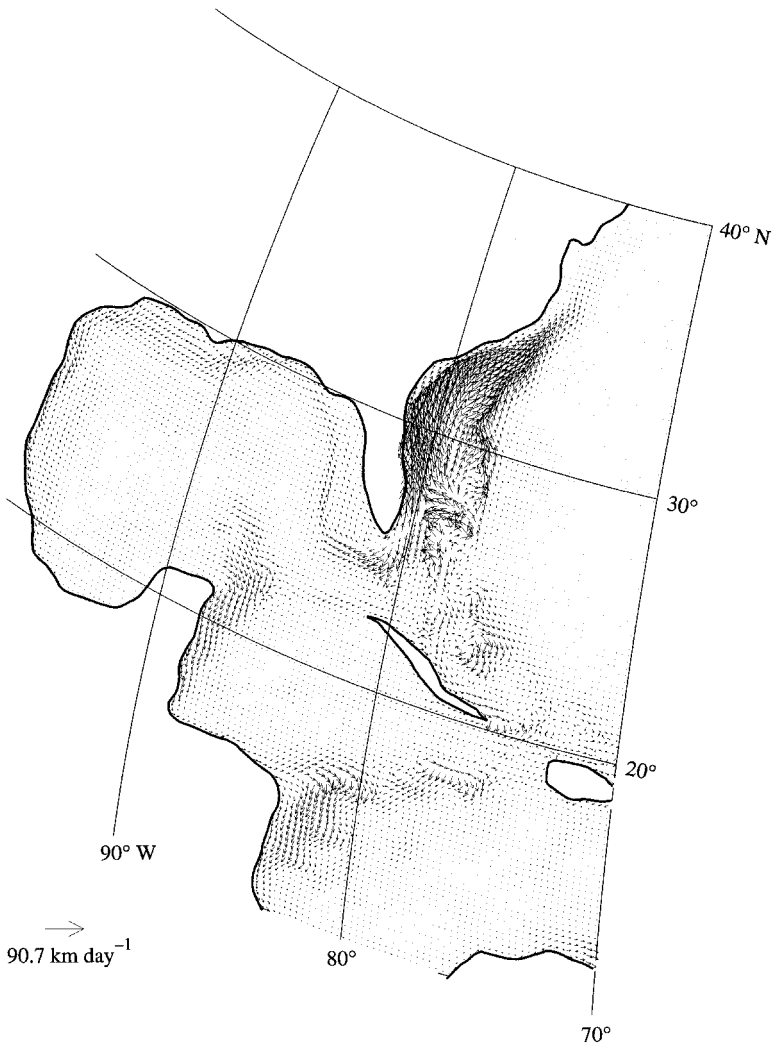
Figure 17. The horizontal velocity at the ocean bottom in the same solution (WWG25) as Figures 14–16. The longest arrow corresponds to a speed of 90.7 km day^{-1}. The bottom-boundary-layer pressure in Figure 16 induces a geostrophic fluid flow that is pseudosouthward—bottom velocity along isobaths with shallow water on the right—throughout the Gulf of Mexico and Caribbean.

large northward geostrophic flow. A similar strong northward flow is present further eastward, along the western edge of the Blake Plateau.

Further southward, the bottom velocity in Figure 17 has a different look. In fact, almost everywhere south of Florida the response to (5.1) is a *pseudosouthward* flow along isobaths, that is, a fluid flow along isobaths with deep water on the left. The explanation for this pseudosouthward flow is the same as for the southward flow at the bottom of Figure 2d.
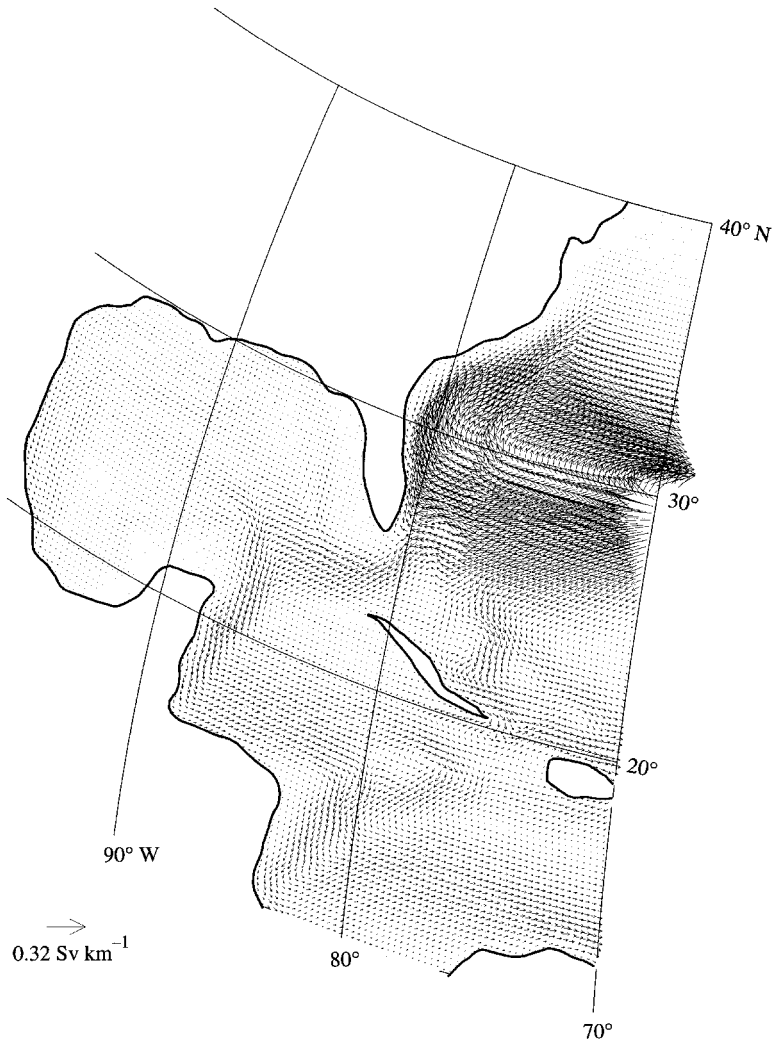
Figure 18. The vertically integrated velocity in the same solution (WWG25) as Figures 14–17. The longest arrow corresponds to a transport of 0.32 Sv per kilometer (of horizontal distance in the direction perpendicular to the arrow). The transport resembles an average of the surface velocity (Fig. 15) and the bottom velocity (Fig. 17). This arrow diagram of transport shows small-scale features much more prominently than the corresponding plot of the streamfunction.

Consider, for example, the "flow" of pressure into the Gulf of Mexico. By the time this "flow" has reached the tip of Florida, the local minimum of pressure near the coastline in Figure 16 has all but disappeared, overwhelmed by "beta advection" from the open-boundary source at 30N. Hence, inside the Gulf of Mexico, the dominant response is a bottom boundary layer with a *positive* correction pressure. The *sign* of this correction

pressure and the *direction* of the bottom slope determine the horizontal pressure gradient and, thereby, the horizontal velocity. This same reasoning explains the strong southward bottom velocity east of Yucatan, Nicaragua, and the Bahamas south of Florida. The surface velocity (Fig. 15) is much more closely confined to the source, but it contains some of the same features as the bottom velocity in coastal regions far from the source (5.1). Th vertically integrated velocity (Fig. 18) resembles an average of the surface and bottom velocities.

Figure 19 is a 527 km section from Florida across the northernmost Bahama Bank at 27N in the same solution, WWG25. The Bank marks the ''upstream'' edge—''upstream'' as regards the ''advection'' of ϕ—of the complicated bathymetry south of Florida. Bottom boundary layers of thickness (4.5) occur near the coast and on the eastern flank of the Bank. These boundary layers are well resolved because the finite elements (Fig. 19, top) concentrate the vertical resolution in shallow water and near the ocean surface and bottom. (In fact, we shall see that the finite elements are capable of resolving bottom boundary layers *twenty-five times* thinner than those in Fig. 19.) These bottom boundary layers carry a strong northward flow (Fig. 19, middle). However, a bottom boundary layer with a relatively small *southward* fluid velocity is present on the *western* flank of the Bank. This boundary layer, which marks the very beginning of the southward bottom flow in the Straits of Florida observed on Figure 17, contains low values of ϕ that have been ''advected'' northward by the ''bottom advection sheet'' on the western flank of the Bank. These low ϕ-values are subsequently ''advected'' clockwise around the north flank of the Bank and thus contribute to the northward fluid velocity on its eastern flank. The overall effect is one of upward doming (Fig. 19, bottom) of the isobars above the Bank, and cyclonic flow around it. (Note that the top of the Bank is a local *maximum* in the bottom pressure (cf. Fig. 16), but a local *minimum* in the pressure at the level of the bank. Thus once again we see that the derivatives of the bottom pressure bear no relation to the geostrophic velocity at the bottom.)

Next we examine a windless western solution, WW25, in which $\varepsilon/\beta = 25$ km, and the open boundary condition is prescribed pressure equal to that obtained in the full-basin solution FB. Thus WW25 differs from WWG25 only in that a boundary pressure resembling Figure 11 (top) replaces the delta function (5.1). (Fig. 11 (top) shows the FB pressure at 70W, whereas the open boundary condition is applied at the heavy line in Fig. 7. There is still no local wind forcing in the western region of interest; hence all the results must still be explicable from the ''advection'' and ''diffusion'' of ϕ. From Figure 11 (top) we see that the new boundary condition differs from (5.1) primarily in that high open-boundary values of ϕ now extend all the way to the coast of South America. Despite this difference, the resulting bottom velocity (Fig. 20) contains many of the features seen in Figure 17. In particular, both figures show a deep counterclockwise flow around the Gulf of Mexico, and strong southward flow in the deep water northeast of Yucatan. The major differences between Figures 17 and 20 are that, in the latter, strong northward flow is present farther southward east of the Bahamas, along the eastern coastlines of Cuba and
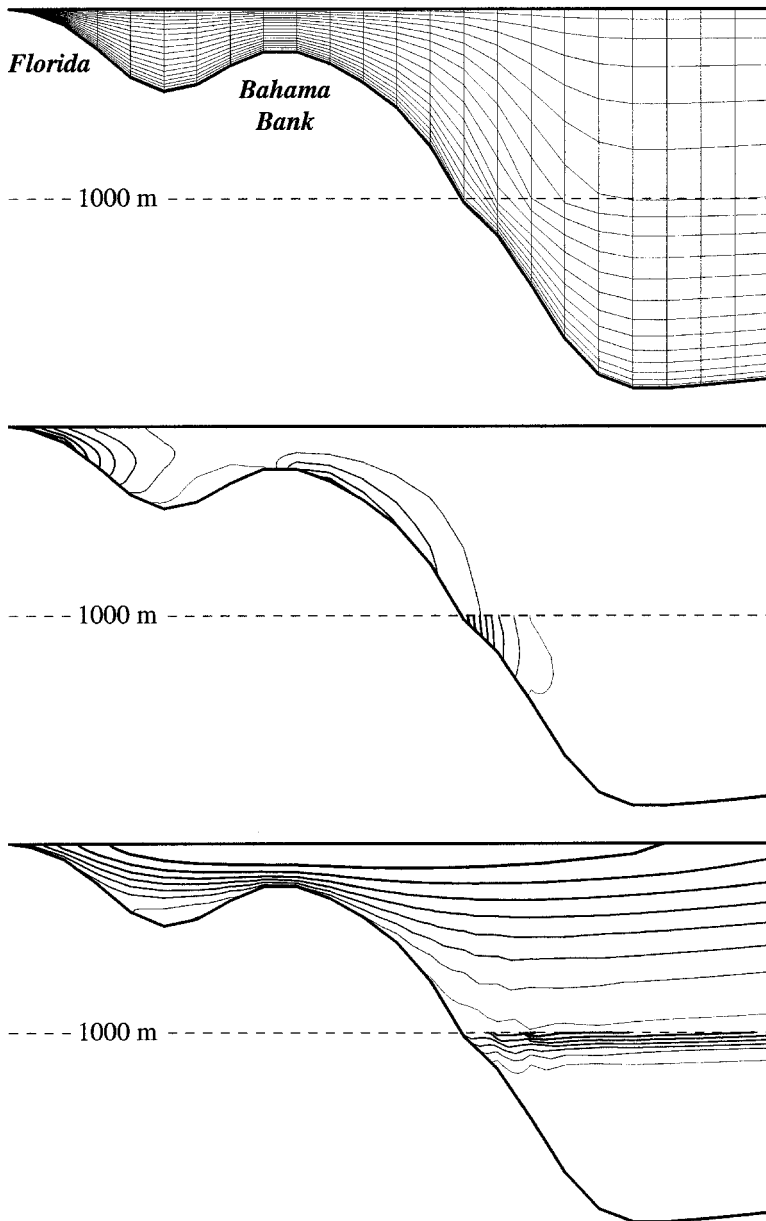
Figure 19. Section along 27N from Florida through the northernmost Bahama Bank in the same solution (WWG25) as Figures 14–18. Once again, the regions above and below 1000 m depth have different vertical scales, and darker contours correspond to larger values. Maximum depth 4770 m. Top: The finite elements. The vertical resolution is greatest in shallow water and near the ocean surface and bottom. Bottom: The pressure ϕ, with shallow contour interval 11.6 cm and deep contour interval 0.16 cm. Middle: Northward velocity, with shallow contour interval 4.02 km day^{-1} and deep contour interval 0.44 km day^{-1}. Range: -5.79 to $+30.4$ km day^{-1}. The "advection" of pressure by the "bottom advection sheet" explains the doming of pressure surfaces over the Bank and the corresponding cyclonic flow within the bottom boundary layer around the Bank.
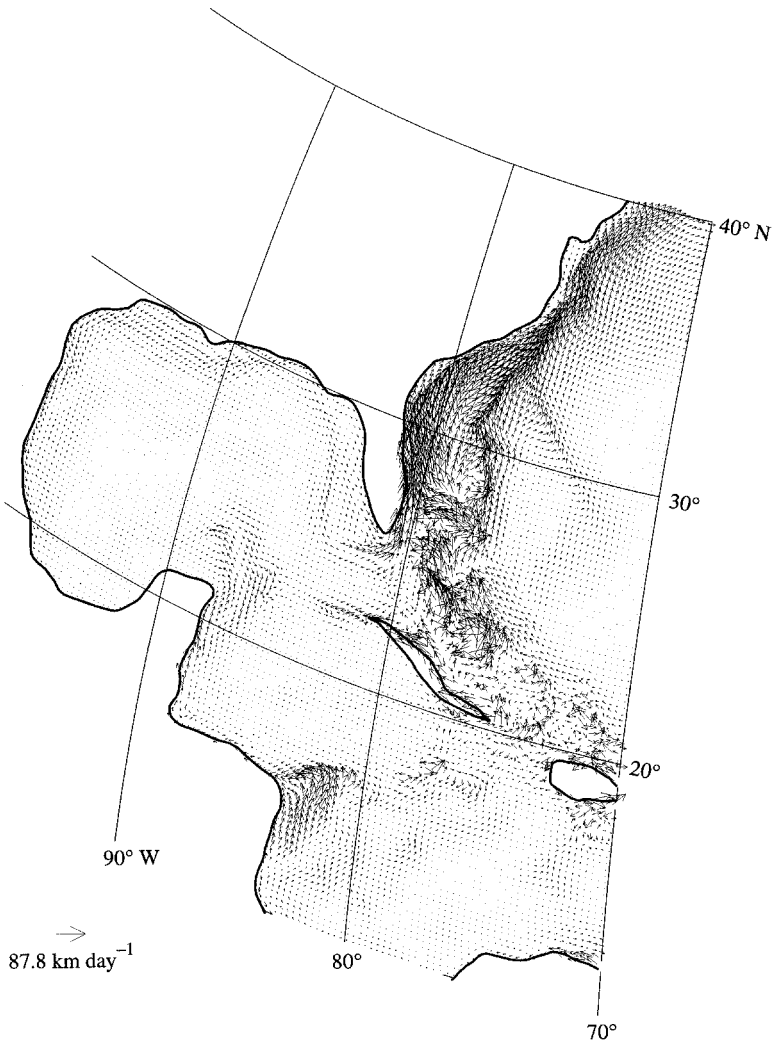
Figure 20. The horizontal velocity at the ocean bottom in the solution WW25 with friction parameter $\varepsilon/\beta = 25$ km, no local wind forcing, and open-boundary condition of pressure ϕ equal to that of the full-basin solution FB. Maximum velocity, 87.8 km day^{-1} (corresponding to an arrow with the size at the lower left). This bottom velocity differs from the bottom velocity in Figure 17 solely because of the different boundary conditions at the open boundary (the heavy line on Fig. 7).

Hispaniola, in the shallow water northeast of Nicaragua, and on the deep eastern flank of Blake ridge (extending southeastward in a straight line from the Carolina coast).

All of these differences are explicable on the basis of a high open-boundary pressure that extends farther to the north and, especially, south than (5.1). For example, the counterclockwise flow around Cuba and Hispaniola (leading to westward flow in the northern halves of

the Windward and Mona Passages) has the same explanation as did the cyclonic bottom flow around the bank at 27N in Figure 19.

To explain the differences between Figures 17 and 20 in the western Caribbean, we consider the westward "beta advection," in WW25, of the high, open-boundary ϕ-values from the latitudes south of Florida, through the passages in the eastern Caribbean. To appreciate this "beta advection" effect we consider a windless western solution, WW1, with the same open-boundary condition as WW25, but with a much smaller friction parameter $\varepsilon/\beta = 1$ km, corresponding to bottom boundary layers twenty-five times thinner than in previous solutions. In this truly asymptotic regime, which tests the finite element code rather severely, the bottom velocity (not shown) qualitatively resembles that of Figure 20, but the maximum bottom velocity rises to 1100 km day^{-1} because of the thinner bottom boundary layer. The surface velocity (Fig. 21) only triples, but it dramatically shows the "beta advection" of high ϕ into the Caribbean and Gulf of Mexico. Most striking in Figure 21 are the long "beta shadows" thrown by the islands of Cuba and Hispaniola, and by the Great Bahama Bank (directly north of Cuba). Inside these shadows, the sea surface is depressed. At the edges of the shadows lie narrow, frictional, internal boundary layers of the kind analyzed by Pedlosky (1996), with strong, zonal, geostrophic velocities arising from the rapid change in sea surface height across the internal boundary layers. By inspection of (3.7), the internal boundary layers have thickness $\sqrt{L\varepsilon/\beta}$, where L is the distance from the beginning of the shadow. For $L = 1000$ km (a representative Caribbean width) and $\varepsilon/\beta = 1$ km, we estimate a maximum internal boundary layer thickness of order 30 km, in agreement with Figure 21. In WW1, the high-ϕ "beam" just north of Cuba and the very broad beam south of Hispaniola cause a strong northward bottom flow (not shown) in WW1 along the coasts of Yucatan and Nicaragua, respectively. These regions of strong northward flow also appear in the bottom velocity of WW25 (Fig. 20), although the higher friction of WW25 blurs the beams considerably, and thus makes the origins of these northward currents less obvious.

Next we examine the details of the full-basin solution FB in the region west of 70W. Once again, the only difference between FB and WW25 is the presence, in the former, of wind forcing—the "source" term W in the ϕ-equation—in the region west of the heavy line in Figure 7. Figure 22, an enlargement of Figure 8, shows the quantity $f\delta_E W_S$, which approximately equals the negative of the wind stress curl, in the region west of 70W. Once again, W_S is the surface value of W; recall (4.3). From Figure 22 we see that the eastern Caribbean is a region of strong negative wind curl (positive W). However, the wind curl is actually positive (W negative) in the very southern Caribbean and the western Gulf of Mexico. Figure 23 shows the bottom velocity in solution FB, which, unlike WW25, feels the "source" shown in Figure 22. The FB bottom velocity of Figure 23 differs from the WW25 bottom velocity in Figure 20 in the presence in FB of: strong anticyclonic flow in the northern Gulf of Mexico; stronger southward flow than in WW25 along the western boundary in the southern Gulf of Mexico; and stronger northward flow in FB northeast of Yucatan and east of Nicaragua. All of these differences are easily understandable from the
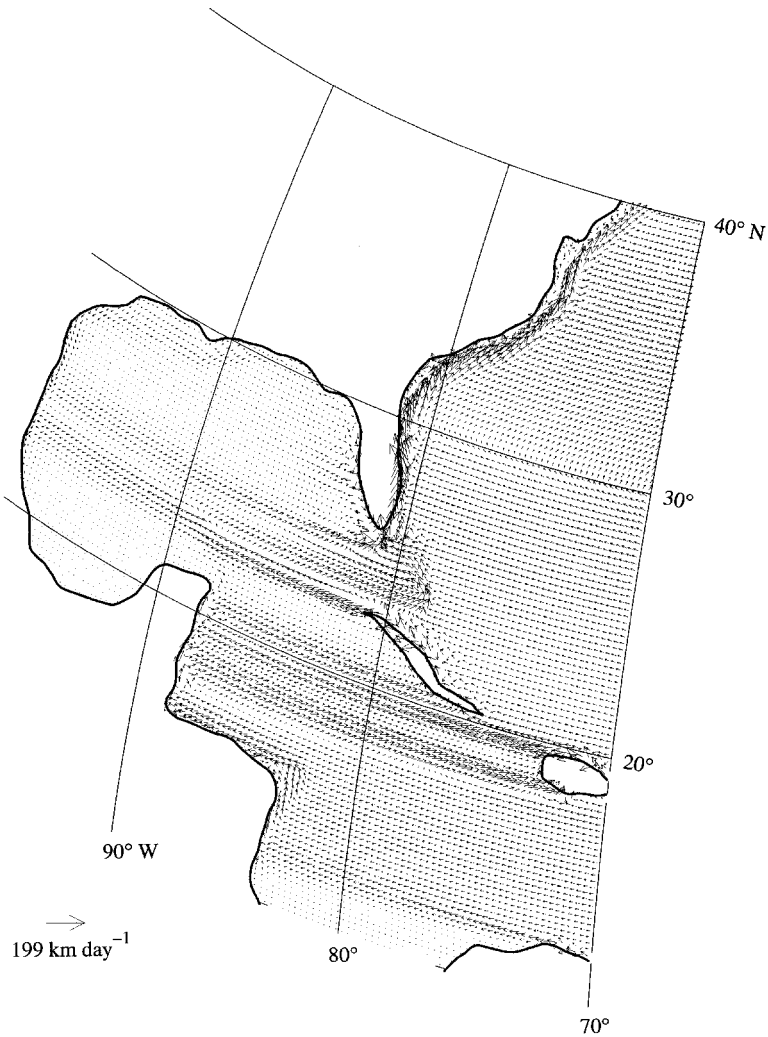
Figure 21. The horizontal velocity at the surface in the solution WW1 with friction parameter $\varepsilon/\beta = 1$ km, no local wind forcing, and open-boundary condition of pressure ϕ equal to that of the full-basin solution FB. Maximum velocity, 199 km day^{-1}. At this low value of friction, and with no local wind forcing, the islands and Great Bahama Bank cast long "beta shadows," with internal boundary layers of high surface velocity at the edges of the shadows.

local wind forcing of Figure 22. These same differences appear in the vertically integrated velocities of FB (Fig. 24) and WW25 (Fig. 25). (The arrow plots of vertically integrated transport show small-scale features that are not apparent in the corresponding plots of streamfunction.) However, in both solutions, the net transport between Florida and Cuba falls far short of the 30 Sv observed, and, similarly, the net transport through the Windward
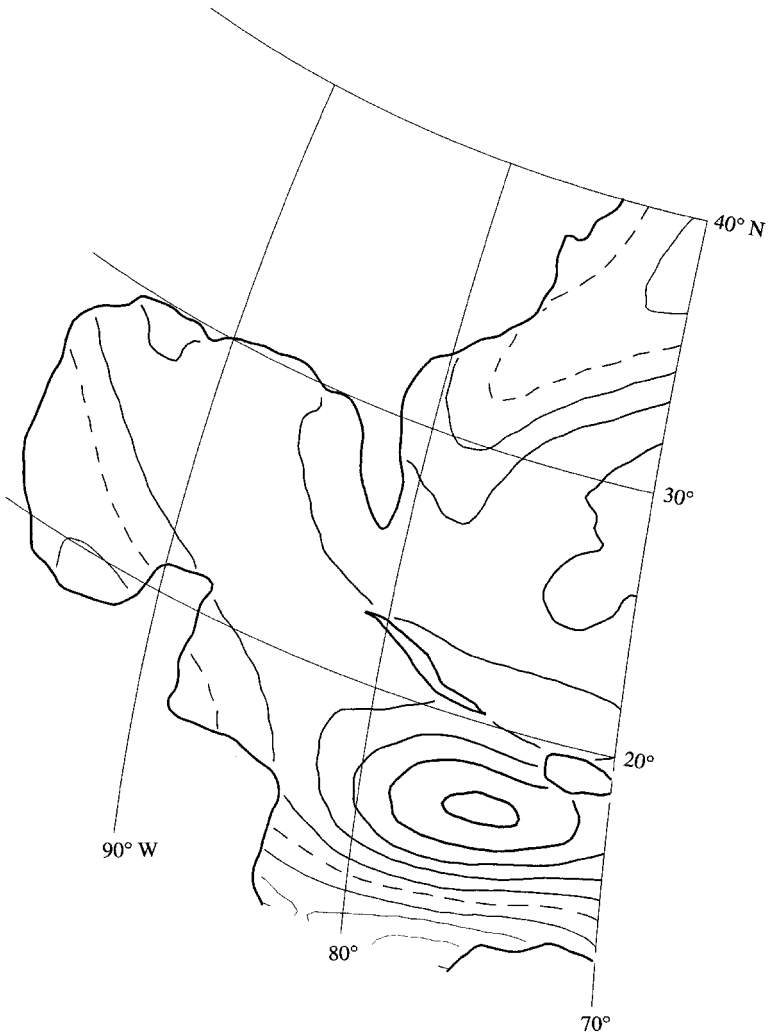
Figure 22. The same as Figure 8, but for the region west of 70W. Contour interval, 2.5×10^{-5} km day^{-2}. The zero contour is dashed.

Passage is well below the 7 Sv proposed by Roemmich (1981) and others. (See Kinder *et al.* (1985) for a review of Caribbean transports.)

Each of Figures 26–28 shows four sections through the Gulf of Mexico and Caribbean in solutions WW1 (Fig. 26), WW25 (Fig. 27), and FB (Fig. 28). These sections offer an interesting view of our results. In the (top) section along 20N, a "ϕ-shadow" is present west of Cuba in the two solutions without local wind forcing (Figs. 26 and 27). However, in the FB solution (Fig. 28) this region contains a thermocline layer that deepens toward the west, much as in Figure 11 (bottom). The (next) section along 15N from Nicaragua, shows
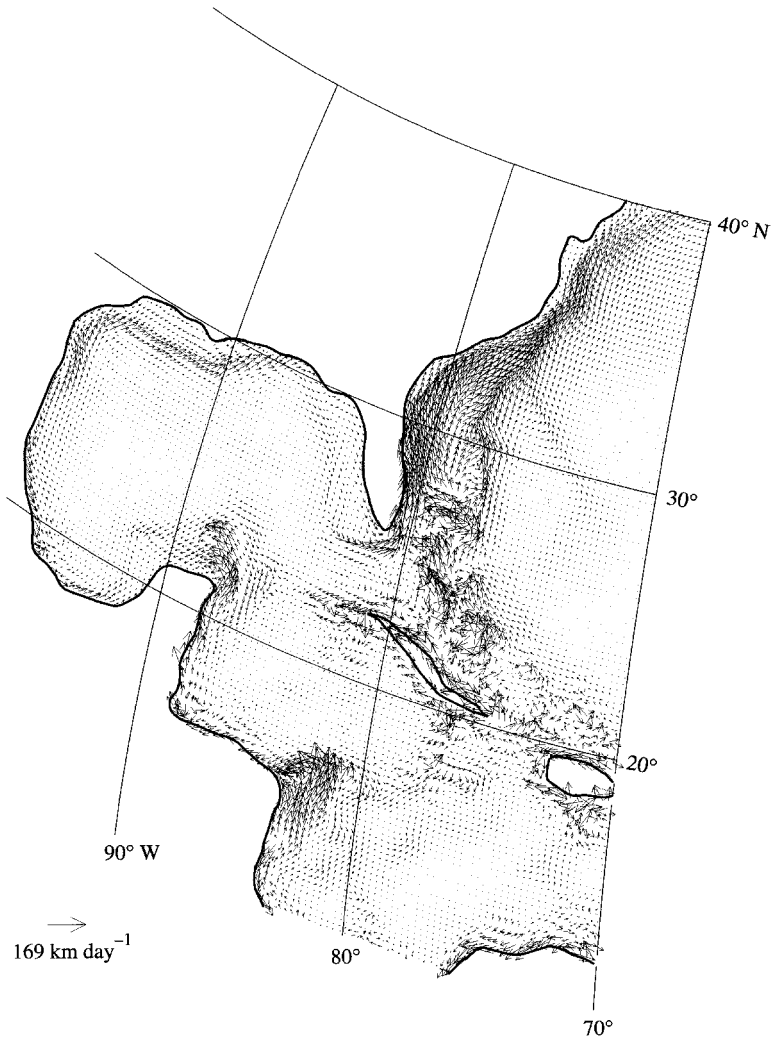
Figure 23. The horizontal velocity at the ocean bottom in the solution FB with wind forcing everywhere. Maximum velocity, 169 km day^{-1}. This bottom velocity differs from that depicted in Figure 20 solely because local wind forcing (shown in Fig. 22) is present in the region west of the heavy line on Figure 7.

how in FB (Fig. 28) the strong Caribbean "source" of ϕ adds to the high values of pressure that are "beta advected" into the Caribbean from the North Atlantic.

In WW1, the low-friction solution without local wind forcing, the pressure along 81W in Figure 26 shows four "beams" of high ϕ. The "shadow" cast by Great Bahama Bank separates the two beams passing between Florida and Cuba. The other two beams have passed through the Windward Passage and through the broad region between Hispaniola and Venezuela. By 90W (Fig. 26, bottom), friction has merged the two Florida Straits
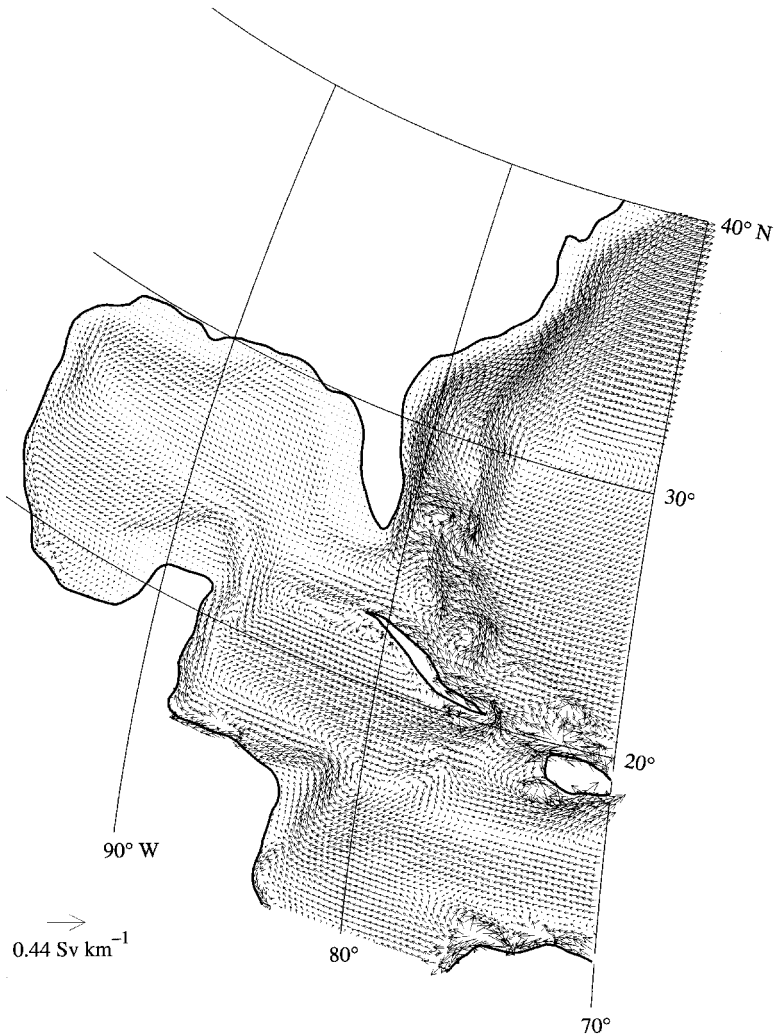
Figure 24. The vertically integrated horizontal velocity in solution FB, which feels the wind forcing over the whole North Atlantic. Maximum transport, 0.44 Sv km^{-1} (corresponding to an arrow with the size at lower left).

beams into a single, but still relatively localized beam. (Note the big difference in horizontal scale between the 81W and 90W sections on Fig. 26.) In the higher-friction solution WW25 (Fig. 27), only two beams are present at 81W, and no beams are visible at 90W. The FB solution (Fig. 28), with the same friction, also shows two beams at 81W, but local wind forcing dominates the solution at 90W.

6. Remarks

In this paper, we have examined the solutions of an especially simple, linear, ocean circulation model, (2.1), with observed wind and realistically complicated bathymetry.
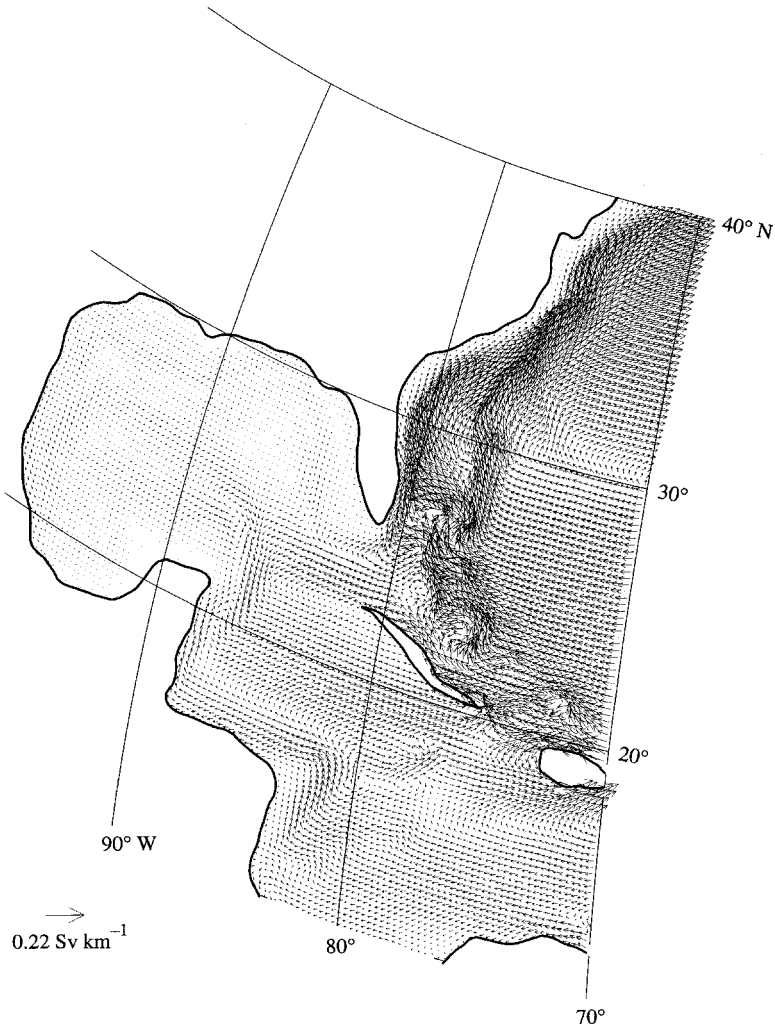
Figure 25. The vertically integrated horizontal velocity in solution WW25, which has no wind forcing west of the heavy line in Figure 7. Maximum transport, 0.22 Sv km^{-1}.

Besides the wind and bathymetry, the model contains only two adjustable constants, ε and k/N^2, and only the friction parameter ε is not tightly constrained by observations. Our solutions have ε-values that are probably unrealistically small. However, this truly asymptotic regime, which could be explored only because of the way in which the finite elements were constructed, is the best source of physical understanding, and other solutions (not presented) with larger, probably more realistic ε-values merely resembled fuzzy versions of the solutions presented.

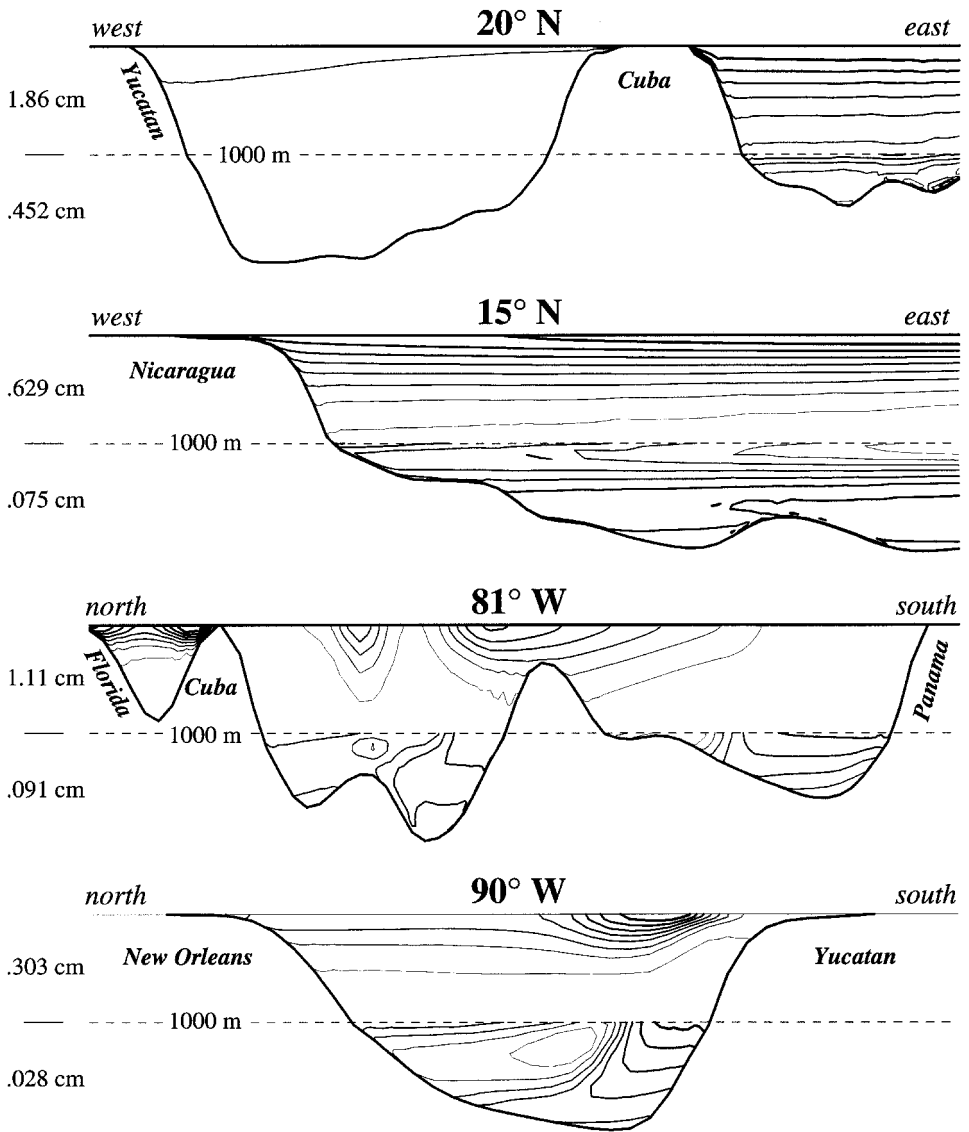Despite the complex bathymetry, we easily explain prominent features of our solutions

Figure 26. Four sections in the Caribbean and Gulf of Mexico, in the solution WW1 with no wind forcing in the western region and very small friction parameter $\varepsilon/\beta = 1$ km. From top to bottom: The pressure ϕ in a section along 20N from Yucatan through Cuba to 70W; along 15N from Nicaragua to 70W, along 81W from Florida to Panama, and along 90W from New Orleans to Yucatan. In each section, the regions above and below 1000 m depth have different vertical scales and contour intervals of pressure. The contour intervals in dynamic cm are shown at the left.
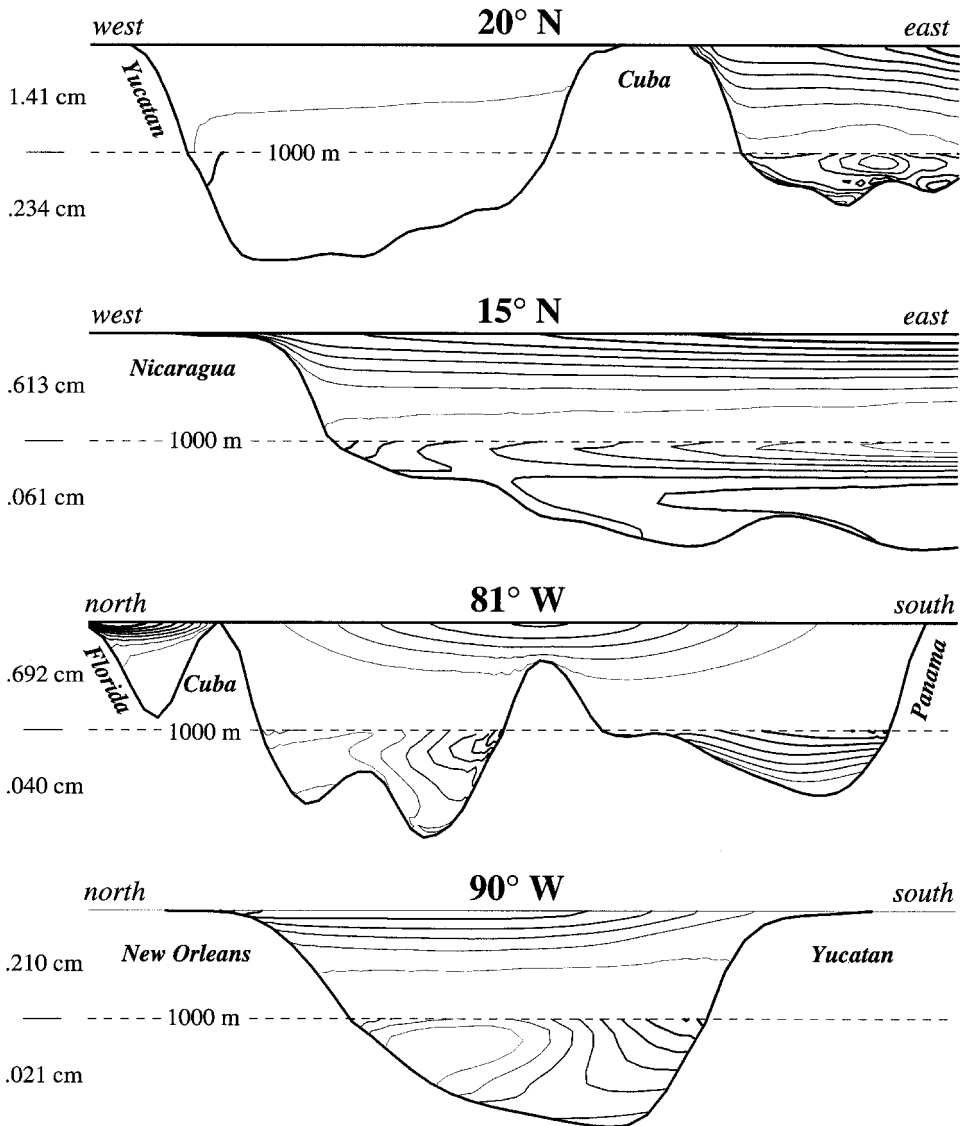
Figure 27. The same as Figure 26, but for the solution WW25 with no wind forcing in the western region, and larger friction parameter $\varepsilon/\beta = 25$ km.

on the basis of the analogy between the equations (2.5, 9, 10) governing the fluid pressure ϕ and the advection-diffusion equation for a passive scalar. In this analogy, the wind curl acts as a "source," and the beta-effect "advects" ϕ westward through the body of the fluid. Along western continental slopes, the bathymetry "advects" ϕ pseudosouthward along isobaths (that is, along isobaths, with shallow water on the right) in a thin layer near the
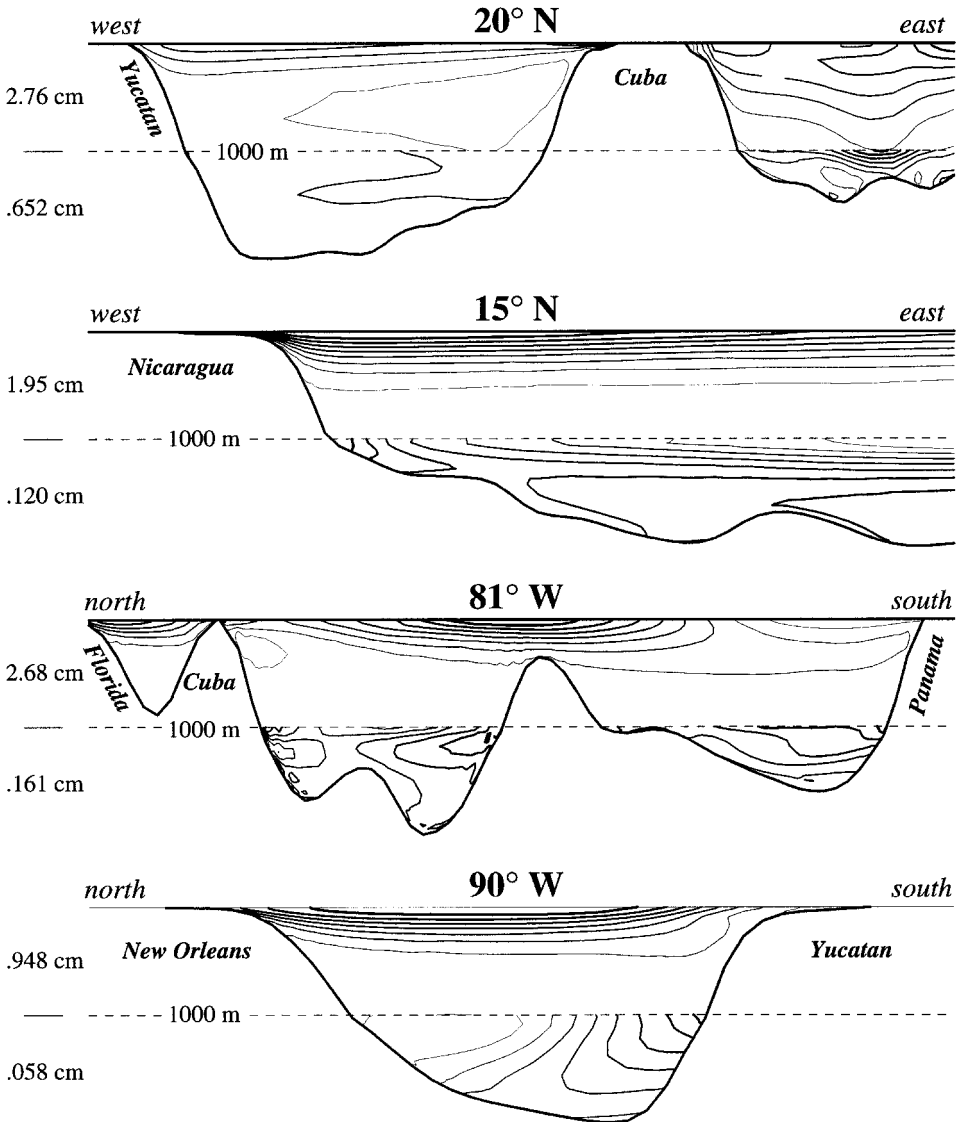
Figure 28. The same as Figures 26 and 27, but for solution FB with wind forcing over the whole North Atlantic, and friction parameter $\varepsilon/\beta = 25$ km.

bottom, producing a pattern of western boundary currents that is very different from the corresponding pattern in a flat-bottom ocean. For example, south of an interior source of high ϕ, the bottom boundary layer pressure on western continental slopes is positive, corresponding to a southward geostrophic fluid velocity. At islands and banks, high interior pressure combined with the clockwise "bathymetric advection" of the low bottom pressures west of the bank produce a cyclonic fluid velocity around the bank.

Unfortunately, neither "beta advection" of pressure in the thin beams between islands and banks, nor "bathymetric advection" of pressure through the Florida Straits can produce a realistically strong model circulation in the Caribbean and Gulf of Mexico. Although observations suggest that nearly half the flow through the Florida Straits originates in the southern hemisphere and is thus prevented by our boundary condition of cross-equatorial symmetry, it is very doubtful that an equatorial boundary condition corresponding to the observed cross-equatorial flow would, in linear theory, lead to a significant improvement. This is because, in linear theory, the "bathymetric advection" of ϕ would directly oppose the penetration of the equatorial pressure signal into the Caribbean Sea, and "beta advection" would merely sweep ϕ into the South American coast. Thus, the weak circulation in the Caribbean Sea seems to be a real failing of linear theory.

In linear theory, strong currents flow along isobaths in either direction; the direction changes with the sign of the wind. In nonlinear theory, advection of momentum or buoyancy leads to rectified flow, in the sense of anticyclonic flow over seamounts, and pseudosouthward flow along western continental slopes. This rectification has been called the "Neptune effect" by Holloway (1992), who favors a statistical mechanical explanation. However, the Neptune effect can also be understood by simple reasoning based on the circulation integral, on potential vorticity mixing, or on the theory of weakly nonlinear waves; see Salmon (1998, pp. 264–273). As noted by Holloway, the deep ocean seems generally to obey the Neptune effect, thus implying a further severe limitation on linear theory.

The greatest deficiency of linear ocean circulation theory is its neglect, in (2.1d), of the horizontal advection of buoyancy. Because of this neglect, the vertical advection of mean buoyancy must be balanced by large buoyancy dissipation. If the dissipation coefficient is too small, then w is too small to produce the vortex stretching that drives the sub-Ekman layer flow. Thus planetary geostrophic dynamics, which includes the full, nonlinear advection of θ, should yield a very significant improvement over linear theory. The present study is a half-way step in the development of a finite-element model based upon the planetary geostrophic equations. Unfortunately, however, nothing as simple as the Welander analogy explains planetary geostrophic dynamics.

APPENDIX ON NUMERICAL METHODS

To define the hexahedrals, we begin with a rectangular grid of nodes on the longitude-latitude plane. At each node, we specify the ocean depth (negative on land). For each node, we define a "region of influence"—a square in latitude and longitude centered on the node. The regions of influence do not overlap. Then, for each node, if the coastline crosses its

region of influence, the node is moved to a location on the coastline. The result is an array of surface nodes whose outside members have been slightly displaced to lie along the coastline. See Figure 13. This method of deforming an initially rectangular grid preserves the property of rectangular grids that the identity of neighboring nodes is easy to determine.

Beneath each surface node we define 19 additional subsurface nodes at prescribed values of the *sigma coordinate* $\sigma \equiv z/H$. Thus there are 20 nodes at each horizontal location. In the idealized solutions of Section 3, all the nodes at a given horizontal location are equally spaced in σ. However, in the North Atlantic solutions described in Sections 4 and 5, the nodes are concentrated near the top and bottom of the ocean, where we expect rapid changes in ϕ, because of the relatively small values of the dissipation parameters in these solutions. The deepest node always lies on the bottom at $\sigma = -1.0$. At coastal locations, where $H = 0$, all the nodes in a vertical column are really the same node. This method of defining nodes concentrates the greatest vertical resolution in the shallowest water, and, in the limit of vanishing depth, is somewhat wasteful of computer storage, but its other advantages seem to outweigh this wastefulness.

In summary, the hexahedral finite elements correspond to a deformed three-dimensional grid. To determine $I[\phi, \alpha]$ and the resulting dynamics, we need only determine the contribution of each hexahedral element to the integral in (4.1). To compute this contribution, it is not even necessary to know whether the element lies within the ocean interior or along the top or bottom boundary. This is a primary advantage of the finite-element method.

Within each element we define *natural coordinates* (ξ, η, ζ) that run from -1 to $+1$ along the edges of the element. Let ϕ^r be the value of ϕ at the r-th node (i.e. corner) of the element, where r runs from 1 and 8. Within the element, we adopt the standard representation

$$\phi = \sum_{r=1}^{8} \phi^r N^r(\xi, \eta, \zeta), \tag{A1}$$

where

$$N^r(\xi, \eta, \zeta) = \tfrac{1}{8}(1 + \xi\xi^r)(1 + \eta\eta^r)(1 + \zeta\zeta^r) \tag{A2}$$

is the *shape function* associated with the r-th node, with coordinates (ξ^r, η^r, ζ^r). The natural coordinates of the 8 element corners are $(\xi^1, \eta^1, \zeta^1) = (-1, -1, -1)$, $(\xi^2, \eta^2, \zeta^2) = (+1, -1, -1)$, etc. Thus $N^r = 1$ at the r-th node, and $N^r = 0$ at all other nodes. This is a simple and very standard finite element representation. Although the representation (A1) of ϕ is continuous between hexahedral elements, the first derivatives of ϕ are discontinuous at the element boundaries.

To determine $I(\phi_1, \phi_2, \ldots, \phi_n, \alpha_1, \alpha_2, \ldots, \alpha_n)$, where n is the number of nodes, we write the contribution of each hexahedral element as an integral over its natural coordinates,

$$I[\phi, \alpha] = \int_{-1}^{+1} \int_{-1}^{+1} \int_{-1}^{+1} d\xi d\eta d\zeta \Bigg\{ \frac{f}{f^2 + \varepsilon^2} J(\phi, \alpha, z) - \frac{\varepsilon}{f^2 + \varepsilon^2} \frac{1}{J(\lambda, \mu, z)}$$

$$\cdot \left(\frac{1}{\cos \mu} J(\phi, \mu, z) J(\alpha, \mu, z) + \cos \mu \, J(\lambda, \phi, z) J(\lambda, \alpha, z) \right) \tag{A3}$$

$$- \frac{r_e^2 \cos \mu}{J(\lambda, \mu, z)} \frac{k}{N^2} J(\lambda, \mu, \phi) J(\lambda, \mu, \alpha) + r_e(u^\tau J(\alpha, \mu, z) + \cos \mu \, v^\tau J(\lambda, \alpha, z)) \Bigg\}$$

where

$$J(A, B, C) \equiv \frac{\partial(A, B, C)}{\partial(\xi, \eta, \zeta)} \tag{A4}$$

is the Jacobian with respect to the natural coordinates. To compute (A3) efficiently, we replace factors in the integrand by their averages over the element. For example, we approximate the first term in (A3) as

$$\iiint d\xi d\eta d\zeta \frac{f}{f^2 + \varepsilon^2} J(\phi, \alpha, z) \approx 8 \left\langle \frac{f}{f^2 + \varepsilon^2} \right\rangle \langle J(\phi, \alpha, z) \rangle. \tag{A5}$$

where $\langle \ \rangle$ denotes the average over the hexahedral, and

$$\langle J(\phi, \alpha, z) \rangle \equiv \tfrac{1}{8} \iiint d\xi d\eta d\zeta \frac{\partial(\phi, \alpha, z)}{\partial(\xi, \eta, \zeta)} = J^{rsp} \phi^r \alpha^s z^p. \tag{A6}$$

The superscripts in (A6) are summed from 1 to 8, and the coefficient

$$J^{rsp} \equiv \tfrac{1}{8} \iiint d\xi d\eta d\zeta \frac{\partial(N^r, N^s, N^p)}{\partial(\xi, \eta, \zeta)} \tag{A7}$$

is computed from (A2). In this way, we finally obtain an approximation to (A3) in the form

$$I = A_{nm} \alpha_n \phi_m + b_n \alpha_n, \tag{A8}$$

leading to the finite-element analogue

$$A_{nm} \phi_m + b_n = 0 \tag{A9}$$

of the equations and boundary conditions for ϕ. In (A8–9) the repeated subscripts are summed over all the nodes. Thus the whole dynamics including boundary conditions correspond to the linear system A9.

Since A_{nm} and b_n require lengthy computations, they must be stored. The North Atlantic solutions described in Sections 4 and 5 have 1,287,780 nodes. Each node has up to 26 nearest neighbors (besides itself). Therefore, A_{nm} and b_n have about 36 million nonzero components, requiring about 144 megabytes of RAM to store.

The solutions of Section 3 (with very smooth, idealized bathymetry) were obtained with

the A_{nm} calculated in exactly the manner described above. However, the corresponding solutions of Sections 4 and 5 (incorporating realistically rough bathymetry) showed unphysical oscillations in the bottom pressure on the scale of the node separation. These oscillations are expected, because the finite-element method described corresponds to second-order-accurate centered differences. (In fact, the oscillations were much smaller than those typically encountered using centered-difference schemes for advection, possibly because the finite element method produces so many linkages between neighboring nodes.) Although these oscillations were relatively small, their effect on the derivatives of pressure (that is, on the fluid velocity and buoyancy) was large near the ocean bottom. The problem was to remove these oscillations without sacrificing accuracy or increasing the storage requirements on A_{nm}. The following method worked much the best of the many alternatives tried.

Let $A_{nm} = J_{nm} + S_{nm}$ where J_{nm} is the antisymmetric matrix arising from the Jacobian term in (4.1), and S_{nm} is the symmetric matrix arising from the ε- and k-terms. Since J_{nm} is antisymmetric, the contribution of the Jacobian terms to $A_{nm}\phi_m$ can be written

$$\sum_m J_{nm}(\phi_m - \phi_n), \qquad (A10)$$

where no summation convention applies. If J_{nm} is positive, then its contribution to (A10) is stabilizing in the sense the J_{nm}-term in (A10) makes a contribution to the diagonal element A_{nn} that has the same sign as the diagonal contributions of the ε- and k-terms in (4.1). Of course, half the terms in (A10) contribute positively to A_{nn} and half contribute negatively; the total contribution of the Jacobian terms to the diagonal of A vanishes by the antisymmetry of J.

To remove the spurious oscillations from the solutions of (A9), I replaced the J_{nm} by

$$\tilde{J}_{nm} = J_{nm} + s|J_{nm}|, \qquad \text{for all} \qquad m \neq n, \qquad (A11)$$

and

$$\tilde{J}_{nn} = -\sum_{m \neq n} s|J_{nm}| \qquad (A12)$$

where s is a constant between zero and unity. That is, in (A10), I increased the stabilizing and decreased the destabilizing terms, by the same percentage. It can be shown (most easily by considering the limit of equally spaced nodes in one dimension) that $s = 1$ corresponds to a first-order upwind approximation to the Jacobian (i.e. "advective") terms in the equation for ϕ. Thus the modification (A11–12) amounts to approximating these "advective" terms by a scheme that is upwind:centered in the ratio $s:(1 - s)$.

First-order upwind differencing ($s = 1$) has a deservedly bad reputation for its high numerical dissipation, but as little as 5% upwind (i.e. $s = 0.05$) proved sufficient to control the spurious oscillations in bottom pressure. However, all of the North Atlantic solutions presented in this paper were computed with a more conservative 15% upwind ($s = 0.15$).

Other solutions with various values of s showed that the solutions do not depend sensitively on s. Nevertheless, s must be considered an additional parameter of the problem (besides ε and k/N^2).

REFERENCES

Becker, J. M. and R. Salmon. 1997. Eddy formation on a continental slope. J. Mar. Res., *55,* 181–200.

Hellerman, S. and M. Rosenstein. 1983. Normal monthly wind stress over the world ocean with error estimates. J. Phys. Oceanogr., *17,* 1093–1104.

Holloway, G. 1992. Representing topographic stress for large-scale ocean models. J. Phys. Oceanogr., *22,* 1033–1046.

Kinder, T. H., G. W. Heburn and A. W. Green. 1985. Some aspects of the Caribbean circulation. Mar. Geol., *68,* 25–52.

Pedlosky, J. 1996. Baroclinic abyssal flow in the presence of a peninsula. J. Phys. Oceanogr., *26,* 2230–2242.

Roemmich, D. 1981. Circulation of the Caribbean Sea: a well-resolved inverse problem. J. Geophys. Res., *86,* 7993–8005.

Salmon, R. 1994. Generalized two-layer models of ocean circulation. J. Mar. Res., *52,* 865–908.

—— 1996. Large-scale semigeostrophic equations for use in ocean circulation models. J. Fluid Mech., *318,* 85–105.

—— 1998. Lectures on Geophysical Fluid Dynamics, Oxford, NY, 378 pp.

Schmitz, W. J. and M. S. McCartney. 1993. On the North Atlantic circulation. Rev. Geophys., *31,* 29–49.

Welander, P. 1968. Wind-driven circulation in one- and two-layer oceans of variable depth. Tellus, *20,* 1–15.